

## Supplementary Information for

### Improved global wetland carbon isotopic signatures support post-2006 microbial methane emission increase

Youmi Oh<sup>1,2,3\*</sup>, Qianlai Zhuang<sup>1,4\*</sup>, Lisa R. Welp<sup>1,5</sup>, Licheng Liu<sup>1,12</sup>, Xin Lan<sup>2,3</sup>, Sourish Basu<sup>6,7</sup>,  
Edward J. Dlugokencky<sup>3</sup>, Lori Bruhwiler<sup>3</sup>, John B. Miller<sup>3</sup>, Sylvia E. Michel<sup>8</sup>, Stefan Schwietzke<sup>9</sup>,  
Pieter Tans<sup>3</sup>, Philippe Ciais<sup>10</sup>, and Jeffrey P. Chanton<sup>11</sup>

<sup>1</sup>Department of Earth, Atmospheric, and Planetary Sciences, Purdue University, West Lafayette, IN, USA.

<sup>2</sup>Cooperative Institute for Research in Environmental Sciences, University of Colorado, Boulder, CO, USA.

<sup>3</sup>Global Monitoring Laboratory, NOAA, Boulder, CO, USA.

<sup>4</sup>Department of Agronomy, Purdue University, West Lafayette, IN, USA.

<sup>5</sup>Purdue Climate Change Research Center, West Lafayette, IN, USA.

<sup>6</sup>Global Modeling and Assimilation Office, NASA Goddard Space Flight Center, Greenbelt, MD, USA.

<sup>7</sup>Earth System Science Interdisciplinary Center, University of Maryland, College Park, MD, USA.

<sup>8</sup>Institute of Arctic and Alpine Research, University of Colorado, Boulder, CO, USA.

<sup>9</sup>Environmental Defense Fund, Berlin, Germany.

<sup>10</sup>Laboratoire des Sciences du Climat et de l'Environnement, 91191 Gif-sur-Yvette, France.

<sup>11</sup>Department of Earth, Ocean, and Atmospheric Sciences, Florida State University, Tallahassee, FL 32306, USA.

<sup>12</sup>Present address: Department of Bioproducts and Biosystems Engineering, University of Minnesota, St. Paul, MN, USA.

\* Authors for correspondence:

Qianlai Zhuang

Email: [qzhuang@purdue.edu](mailto:qzhuang@purdue.edu)

Youmi Oh

Email: [youmi.oh@noaa.gov](mailto:youmi.oh@noaa.gov)

Under Review: *Communications Earth & Environment*

Contents of this file: Supplementary figures 1 to 30, supplementary tables 1 to 11, and 34 references

## Supplementary Figure Captions

**Supplementary Figure 1. Global map of C<sub>4</sub> fraction of vegetation from Still *et al.* (2003)<sup>1</sup>.**

**Supplementary Figure 2. Simulation of instantaneous and cumulative  $\delta^{13}\text{C}$ -POM for wetland soils as an example with no C<sub>4</sub> plant fraction.** We set the initial  $\delta^{13}\text{C}$ -POM in 1851 based on the global C<sub>3</sub> and C<sub>4</sub> vegetation distribution (Supplementary Fig. 1)<sup>1</sup> by setting -27 and -13‰ for C<sub>3</sub>- and C<sub>4</sub>-only vegetation area. The instantaneous  $\delta^{13}\text{C}$ -POM depends on long-term changes in atmospheric  $\delta^{13}\text{C}$ -CO<sub>2</sub> from Graven *et al.* (2017)<sup>2</sup>. We applied latitude-dependent seasonality of  $\delta^{13}\text{C}$ -CO<sub>2</sub> based on seasonality of atmospheric  $\delta^{13}\text{C}$ -CO<sub>2</sub> from ALT and SPO (<https://gml.noaa.gov/dv/data/>), and set the minimum at 90 °S (panel a) and maximum seasonality at 90 °N (panel b). Cumulative  $\delta^{13}\text{C}$ -POM depends on  $\delta^{13}\text{C}$ -POM of the previous year and changes in instantaneous  $\delta^{13}\text{C}$ -POM with a 6-year carbon residence time between photosynthesis and methane production in the biosphere<sup>3</sup>. Shaded area represents standard deviation from Graven *et al.* (2017)<sup>2</sup>.

**Supplementary Figure 3. Results of regressions between fraction of hydrogenotrophic methanogens (HM) and (a) latitude, (b) pH, and (c) total soil carbon. Global pH and total soil carbon data are from the Harmonized World Soil Database<sup>4</sup>.**

**Supplementary Figure 4. Calibration results of seasonal methane emissions in  $\text{mg m}^{-2} \text{day}^{-1}$  (a,b,e,f,i,j) and its carbon isotope changes in  $\delta^{13}\text{C}$ -CH<sub>4</sub> (c,d,g,h,k,l) for forested (a,c,e,g,i,k) and non-forested (b,d,f,h,j,l) systems in boreal (a-d), temperate (e-h), and tropical (i-l) regions.** Red error bars represent observations with their standard deviations, and blue lines are simulation results. The observations in panel j and j represent diffusive-only fluxes while the model simulates other pathways, therefore there are discrepancies.

**Supplementary Figure 5. Global soil wetland and vegetation map.** (a) Default wetland type map from Matthews and Fung (1987)<sup>5</sup>, where type 1 and 2 represent forested and non-forested bog, type 3 and 4 represent forested and non-forested swamp, and 5 represents alluvial wetlands. The wetland map was developed based on vegetation, soil properties, and fractional inundation, and it yielded a global distribution of wetland sites identified with in situ ecological and environmental characteristics. (b) Filled wetland type map. For sites without wetland types in panel a, we assigned forested soils for type 1 and non-forested soils for type 2 based on the global vegetation distribution in panel c. (c) Global vegetation distribution<sup>6</sup>, where

numbers 1-35 represent ice, alpine tundra & polar desert, wet tundra, boreal forest, forested boreal wetlands, boreal woodlands, non-forested boreal wetlands, mixed temperate forests, temperate coniferous forests, temperate deciduous forests, temperate forested wetlands, tall grasslands, short grasslands, tropical savannas, xeric shrublands, tropical evergreen forests, tropical forested wetlands, tropical deciduous forests, xeric woodlands, tropical forested floodplains, deserts, tropical non-forested wetlands, tropical non-forested floodplains, temperate non-forested wetland, temperate forested floodplains, temperate non-forested floodplains, wet savannas, salt marsh, mangroves, tidal freshwater marshes, temperate savannas, cultivation, temperate evergreen broadleaf, unknown, and mediterranean shrublands, respectively.

**Supplementary Figure 6. Simulated wetland fluxes with (a) static inundation data from Matthews and Fung (1987)<sup>5</sup> and (b) transient inundation data from Poulter *et al.* (2017)<sup>7</sup>, and (c) their latitudinal sum of fluxes with static (blue) and transient (red) inundation data in 2000.**

**Supplementary Figure 7. Global distribution of wetland  $\delta^{13}\text{C-CH}_4$  and its latitudinal gradients simulated by isoTEM. (a) Modeled global wetland  $\delta^{13}\text{C-CH}_4$  for wetland grid cells with dynamic inundation data (Poulter *et al.*, 2017<sup>7</sup>). (b) Mean latitudinal distribution of wetland  $\delta^{13}\text{C-CH}_4$ .**

**Supplementary Figure 8. Global map of wetland  $\delta^{13}\text{C-CH}_4$  by (a) isoTEM in July, 2000 and (b) Ganesan *et al.* (2018)<sup>8</sup>, and (c) their latitudinal mean of  $\delta^{13}\text{C-CH}_4$  by isoTEM (blue) and Ganesan *et al.* (2018)<sup>8</sup> (red). The shaded area represents in panel c one standard deviation determined from 20 ensemble simulations where the optimized parameters were varied.**

**Supplementary Figure 9. Histograms of modeled global wetland  $\delta^{13}\text{C-CH}_4$  by (a) Ganesan *et al.* (2018)<sup>8</sup>, and isoTEM with (b) all grid cells and (c) wetland cells only. Red lines represent mean of wetland  $\delta^{13}\text{C-CH}_4$ .**

**Supplementary Figure 10. Seasonality of (a) mean  $\delta^{13}\text{C-CH}_4$  and (b) sum of methane fluxes for global (blue), boreal (green), temperate (yellow), and tropic (red) regions with static inundation data<sup>5,9</sup>. Shaded area in (a) represents one standard deviation by varying the optimized parameters from ensemble simulations. Blue in panel a represents flux-weighted global  $\delta^{13}\text{C-CH}_4$ . At grid and regional scale, the small seasonal variability of  $\delta^{13}\text{C-CH}_4$  has been shown in other literature<sup>10-12</sup>. Studies also pointed out the**

uncertainty in seasonality of  $\delta^{13}\text{C-CH}_4$ <sup>13</sup>, and the contrasting seasonality for Arctic<sup>12,13</sup>, temperate<sup>11,14</sup>, and tropical wetlands<sup>15,16</sup>.

**Supplementary Figure 11. Global map of 70 wetlands sites used for site-level comparison of wetland  $\delta^{13}\text{C-CH}_4$ .** All observation data used for site-level comparison are listed in Supplementary Data 1.

**Supplementary Figure 12. Site-level model-data comparison.** (a-c) Comparison of observations with (a) Ganesan et al. (2018), (b) isoTEM in July 2016, and (c) temporally-varying isoTEM and (d-f) their histograms of the differences between each model and observations from tropic (red), temperate (yellow), and boreal (blue) regions. Error bars in panel a-c represent one standard deviation of measured wetland  $\delta^{13}\text{C-CH}_4$ . All observation data used for site-level comparison are listed in Supplementary Data 1 and Supplementary Figure 11.

**Supplementary Figure 13. Miller-Tans plots of airborne measurements in (a-c) 2012, (d-f) 2013, and (g-i) 2015 for (a,d,g) North Slope, (b,e,h) interior, and (c,f,i) southwest Alaska.** The left figure of each panel shows curve fitting of Miller-Tans plot<sup>17</sup>, where the slope of the fit represents an estimated source signature of wetland  $\delta^{13}\text{C-CH}_4$ . The right figure of each panel shows data location and  $\text{CH}_4$  mole fraction. The Alaskan maps are generated using a ‘worldmap’ function in Matlab<sup>18</sup>.

**Supplementary Figure 14. Spatial map of  $\delta^{13}\text{C}$  simulated in isoTEM in July, 2000.** Map of  $\delta^{13}\text{C}$  of (a) precursor organic matter, (b) produced  $\text{CH}_4$ , (c) oxidized  $\text{CH}_4$ , and (d)  $\text{CH}_4$  emitted to the soil surface.

**Supplementary Figure 15. Long-term trends of wetland  $\delta^{13}\text{C-CH}_4$  simulated without long-term trend of  $\delta^{13}\text{C}_{\text{POM}}$  (maroon), and the fraction of plant-mediated transport over all three transport processes (green) for (a) global scale, (b) boreal, (c) temperate, and (d) tropical regions.**

**Supplementary Figure 16. Spatial and temporal variability of the fraction of oxidation, and transport processes.** (a-d) Map of the fraction of (a) oxidation, (b) diffusion, (c) ebullition, and (d) plant-mediated transport. (e) global monthly variability of the fraction of oxidation (blue), diffusion (red), ebullition (yellow), and plant-mediated transport (purple) (Equation 18).

**Supplementary Figure 17. Results of regressions between wetland  $\delta^{13}\text{C-CH}_4$  and year.**

**Supplementary Figure 18. Changes in active layer depth (ALT) simulated by ORCHIDEE-PEAT<sup>19</sup>, under the RCP8.5 scenario.** (a) ALT in July 1986, (b) ALT in July 2016, and (c) differences in ALT between July 2016 and July 1986.

**Supplementary Figure 19. Bottom-up inventory for each source category for Scenarios A-D<sup>5</sup>.** Bottom-up emissions for each category for (a) Scenarios A-B, (b) Scenario C, and (c) Scenario D. The data sources are listed in Supplementary Table 6. Information about Scenarios A-D is in Table 1.

**Supplementary Figure 20. Observed and simulated normalized north-south annual mean gradient of atmospheric  $\delta^{13}\text{C-CH}_4$  for scenarios A-C.** The north-south  $\delta^{13}\text{C-CH}_4$  was calculated by zonally-averaging the surface  $\delta^{13}\text{C-CH}_4$  and normalized based on the  $\delta^{13}\text{C-CH}_4$  at 60-90 °S for (a) 2000, (b), 2006, and (c) 2012. The shaded gray area for observation is formed from 100 data extension and integration surfaces within each of the uncertainty metrics such as network, atmospheric, and bias. The north-south gradient of atmospheric  $\delta^{13}\text{C-CH}_4$  for other years is in Supplementary Table 7. Information about scenarios A-C is in Table 1.

**Supplementary Figure 21. Map of 10 observations sites for atmospheric  $\delta^{13}\text{C-CH}_4$  measurements.** More information about observation sites is in Supplementary Table 10. The Alaskan maps are generated using a ‘worldmap’ function in Matlab<sup>18</sup>.

**Supplementary Figure 22. Histogram of the differences between simulated and observed  $\delta^{13}\text{C-CH}_4$  (in ‰) for Scenarios A-C.** The observed  $\delta^{13}\text{C-CH}_4$  is from 10 NOAA/INSTAAR surface flask measurement sites during the entire observation period listed in Supplementary Table 8. Information about scenarios A-C is in Table 1.

**Supplementary Figure 23. Normalized (a) long-term trend of globally averaged atmospheric  $\delta^{13}\text{C}$ - $\text{CH}_4$  and (b-c) north-south annual mean gradient of atmospheric  $\delta^{13}\text{C}$ - $\text{CH}_4$ .** Scenario C (blue) is the same in Figure 4 and Table 1, and Scenario C without long-term wetland  $\delta^{13}\text{C}$ - $\text{CH}_4$  (purple) removed long-term decrease trend in wetland  $\delta^{13}\text{C}$ - $\text{CH}_4$  of  $\sim 0.6\text{‰}$  during 1984-2016. The long-term trend is normalized based on the global mean  $\delta^{13}\text{C}$ - $\text{CH}_4$  in 1998, and the north-south gradient is normalized based on the  $\delta^{13}\text{C}$ - $\text{CH}_4$  at 60-90 °S for (b) 2006, and (c) 2012.

**Supplementary Figure 24. Bottom-up inventory for each source category for Scenario C with anthropogenic microbial increase.** The data sources are listed in Supplementary Table 8.

**Supplementary Figure 25. Normalized (a) long-term trend of globally averaged atmospheric  $\delta^{13}\text{C}$ - $\text{CH}_4$  and (b-c) north-south annual mean gradient of atmospheric  $\delta^{13}\text{C}$ - $\text{CH}_4$ .** Scenario C (blue) is the same in Figure 4 and Table 1, and the annual emission setup of Scenario C with anthropogenic microbial increase (maroon) during 1984-2016 is in Supplementary Figure 24. The long-term trend is normalized based on the global mean  $\delta^{13}\text{C}$ - $\text{CH}_4$  in 1998, and the north-south gradient is normalized based on the  $\delta^{13}\text{C}$ - $\text{CH}_4$  at 60-90 °S for (b) 2006, and (c) 2012.

**Supplementary Figure 26. Latitudinal gradients of wetland  $\text{CH}_4$  emission for scenarios E-H with transient inundation data<sup>7</sup>.** Latitudinal gradients of total wetland  $\text{CH}_4$  emissions for scenarios E/F (red), G (blue), and H (purple) for (a) 2000, (b) 2010, and (c) 2015. Information about scenarios E-H is in Supplementary Table 11.

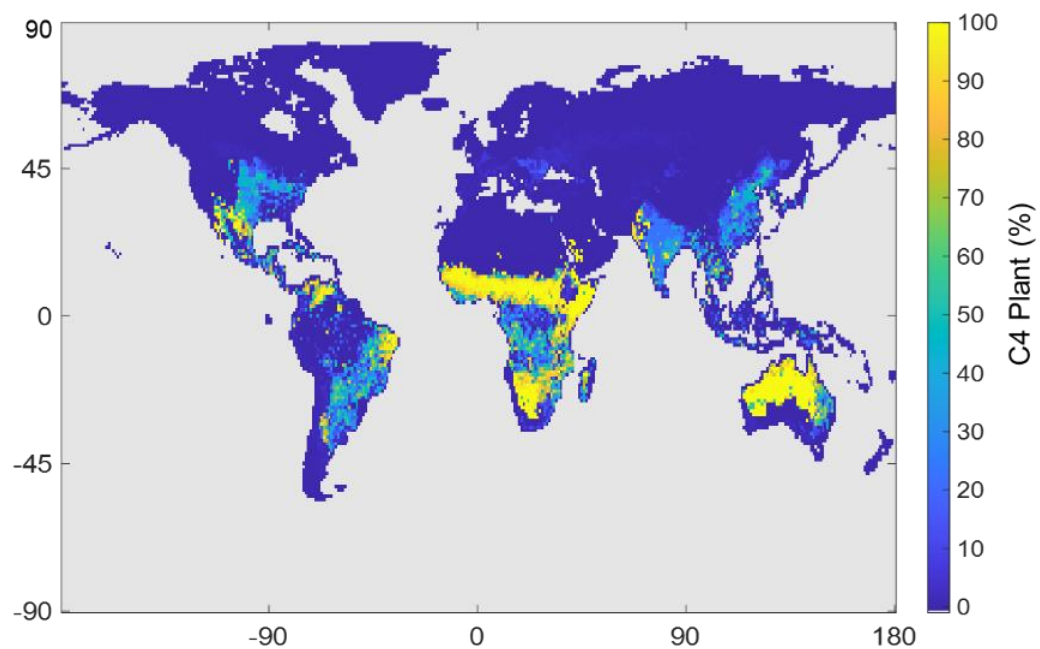
**Supplementary Figure 27. Bottom-up inventory for each category for Scenarios E-H with transient inundation data<sup>7</sup>.** Bottom-up emissions for each category for (a) Scenario E/F, (b) Scenario G, and (c) Scenario H with transient inundation data from Poulter et al. (2017)<sup>7</sup>. The data sources are listed in Supplementary Table 7 and the scenario information is listed in Supplementary Table 11.

**Supplementary Figure 28. Long-term trend of globally averaged atmospheric  $\text{CH}_4$  and  $\delta^{13}\text{C}$ - $\text{CH}_4$  for Scenarios E-H.** Model-data comparison of long-term trend of atmospheric  $\text{CH}_4$  (in ppb) and  $\delta^{13}\text{C}$ - $\text{CH}_4$  (in ‰) by observation (grey) and simulations from Scenario E (yellow), F (red), G (blue), and H (purple) with

transient inundation from Poulter et al. (2017)<sup>7</sup>. The shaded gray area for observation is formed from 100 data extension and integration surfaces within each of the uncertainty metrics such as network, atmospheric, and bias. Information about scenarios E-H are in Supplementary Table 11.

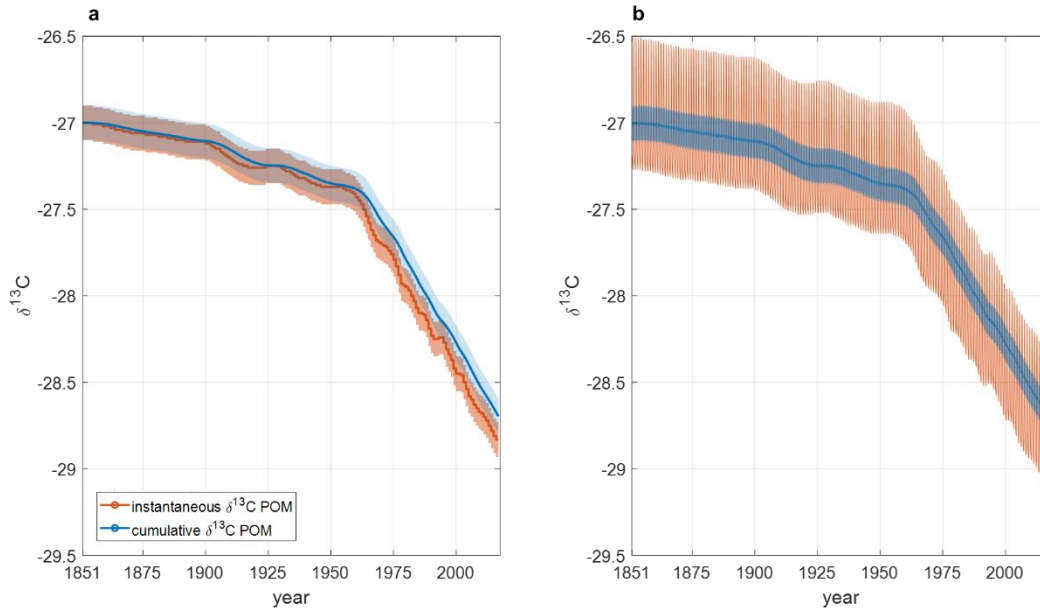
**Supplementary Figure 29. Observed and simulated normalized north-south annual mean gradient of atmospheric  $\delta^{13}\text{C-CH}_4$  for scenarios E-H.** The north-south  $\delta^{13}\text{C-CH}_4$  was calculated by zonally-averaging the observed and simulated surface  $\delta^{13}\text{C-CH}_4$  and normalized based on the  $\delta^{13}\text{C-CH}_4$  at 60-90 °S for (a) 2000, (b) 2006, and (c) 2012 for Scenario E (yellow), F (red), G (blue), and H (purple). The shaded gray area for observation is formed from 100 data extension and integration surfaces within each of the uncertainty metrics such as network, atmospheric, and bias. Information about scenarios E-H are in Supplementary Table 11.

**Supplementary Figure 30. Histogram of the differences between simulated and observed  $\delta^{13}\text{C-CH}_4$  for Scenarios E-H.** The observed  $\delta^{13}\text{C-CH}_4$  is from 10 NOAA/INSTAAR surface flask measurement sites during the entire observation period listed in Supplementary Table 8. Information about scenarios E-H is in Supplementary Table 11.

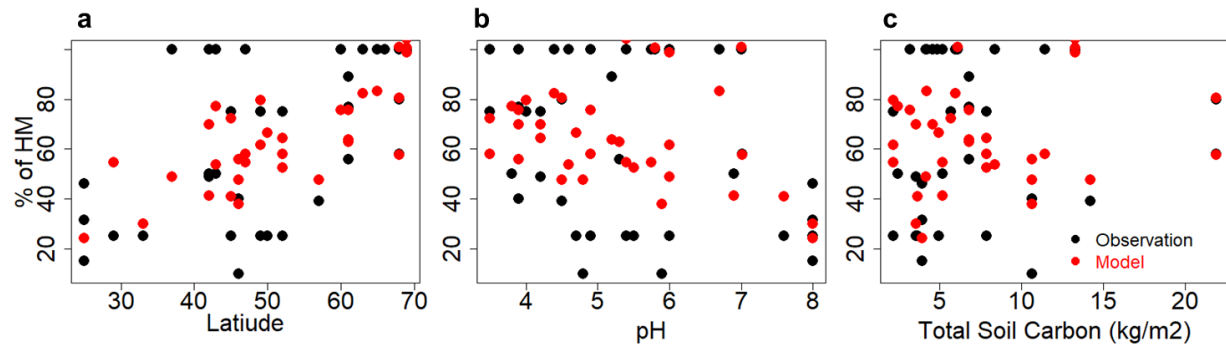


**Supplementary Figure 1. Global map of C<sub>4</sub> fraction of vegetation from Still *et al.* (2003)<sup>1</sup>.**

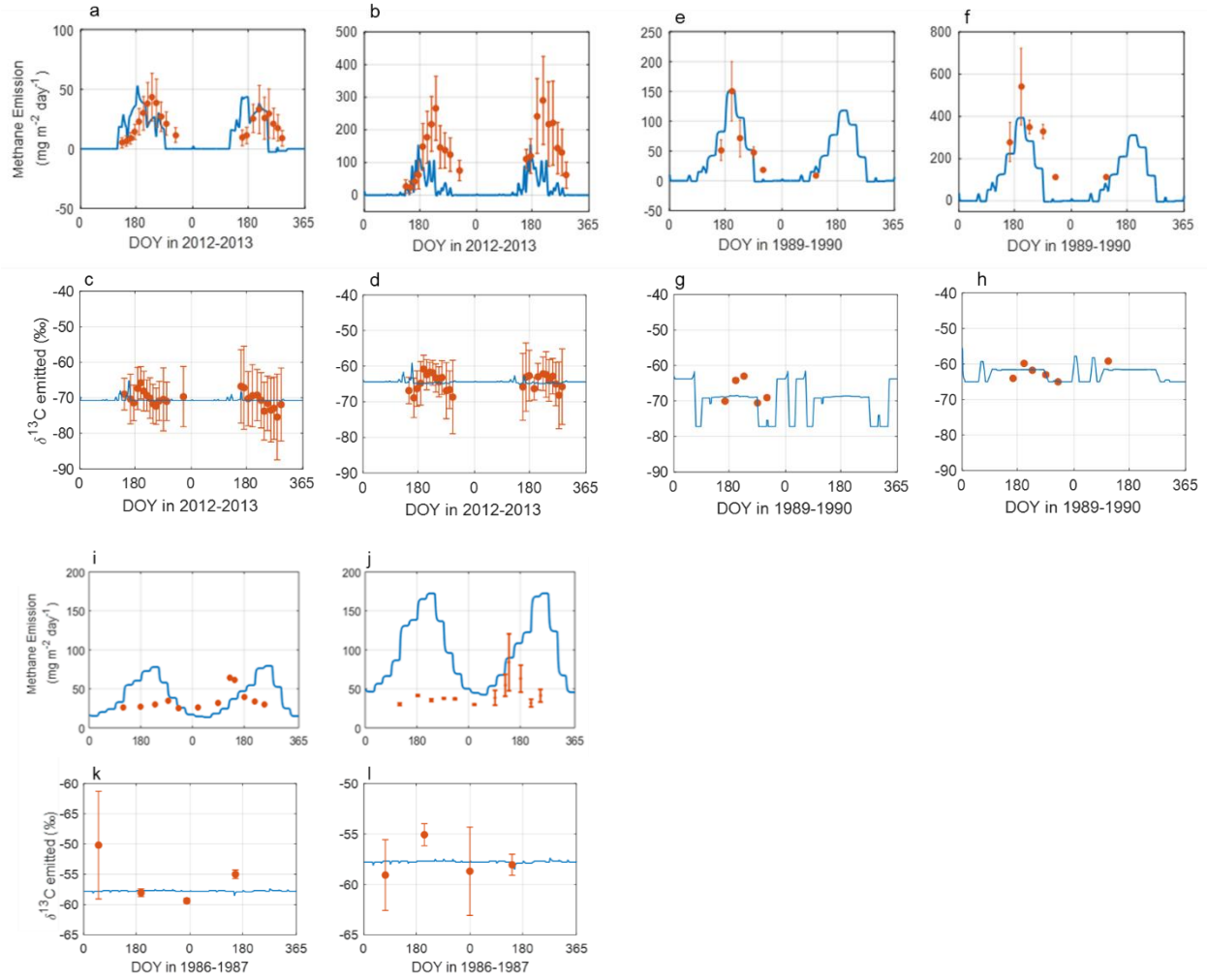




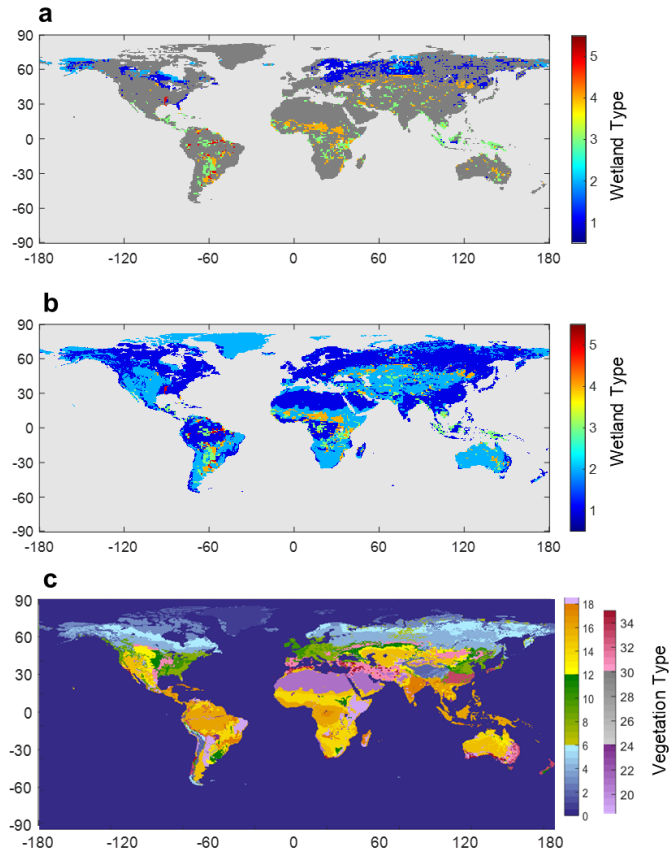
**Supplementary Figure 2. Simulation of instantaneous and cumulative  $\delta^{13}\text{C}$ -POM for wetland soils as an example with no  $\text{C}_4$  plant fraction.** We set the initial  $\delta^{13}\text{C}$ -POM in 1851 based on the global  $\text{C}_3$  and  $\text{C}_4$  vegetation distribution (Supplementary Fig. 1)<sup>1</sup> by setting -27 and -13‰ for  $\text{C}_3$ - and  $\text{C}_4$ -only vegetation area. The instantaneous  $\delta^{13}\text{C}$ -POM depends on long-term changes in atmospheric  $\delta^{13}\text{C}$ - $\text{CO}_2$  from Graven *et al.* (2017)<sup>2</sup>. We applied latitude-dependent seasonality of  $\delta^{13}\text{C}$ - $\text{CO}_2$  based on seasonality of atmospheric  $\delta^{13}\text{C}$ - $\text{CO}_2$  from ALT and SPO (<https://gml.noaa.gov/dv/data/>), and set the minimum at 90 °S (panel a) and maximum seasonality at 90 °N (panel b). Cumulative  $\delta^{13}\text{C}$ -POM depends on  $\delta^{13}\text{C}$ -POM of the previous year and changes in instantaneous  $\delta^{13}\text{C}$ -POM with a 6-year carbon residence time between photosynthesis and methane production in the biosphere<sup>3</sup>. Shaded area represents standard deviation from Graven *et al.* (2017)<sup>2</sup>.



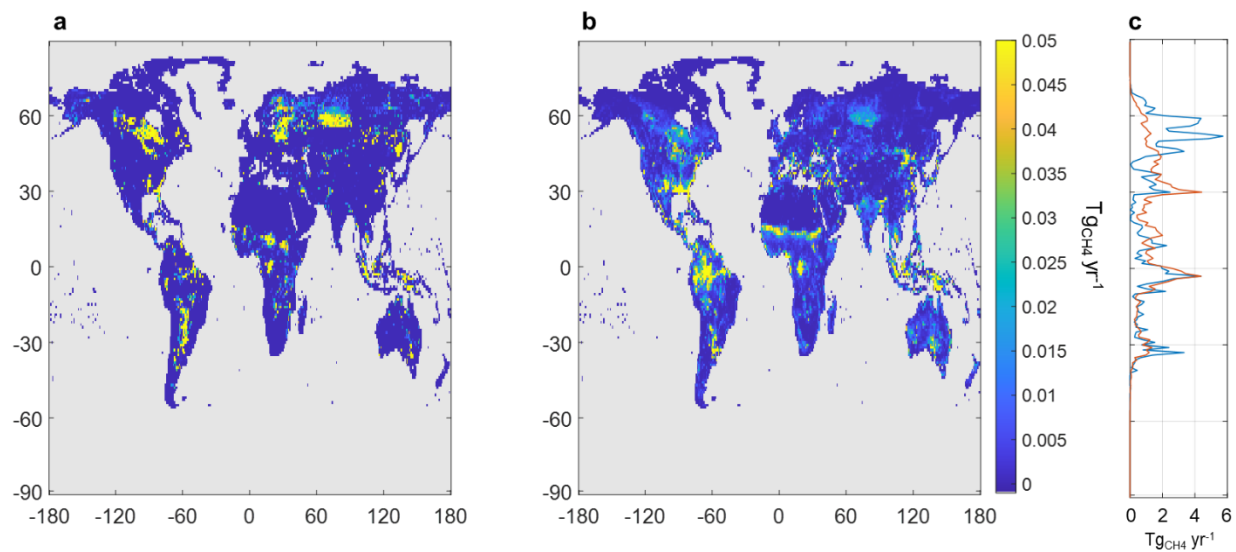
**Supplementary Figure 3. Results of regressions between fraction of hydrogenotrophic methanogens (HM) and (a) latitude, (b) pH, and (c) total soil carbon. Global pH and total soil carbon data are from the Harmonized World Soil Database<sup>4</sup>.**



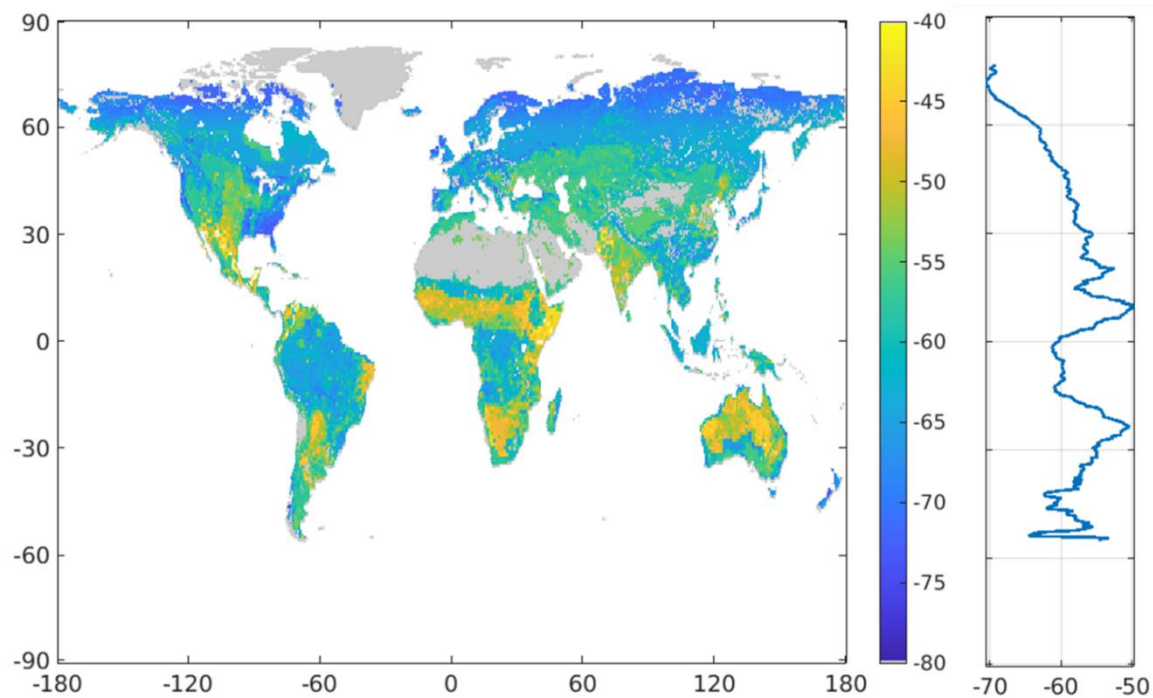
**Supplementary Figure 4. Calibration results of seasonal methane emissions in  $\text{mg m}^{-2} \text{day}^{-1}$  (a,b,e,f,i,j) and its carbon isotope changes in  $\delta^{13}\text{C-CH}_4$  (c,d,g,h,k,l) for forested (a,c,e,g,i,k) and non-forested (b,d,f,h,j,l) systems in boreal (a-d), temperate (e-h), and tropical (i-l) regions. Red error bars represent observations with their standard deviations, and blue lines are simulation results. The observations in panel j and j represent diffusive-only fluxes while the model simulates other pathways, therefore there are discrepancies.**



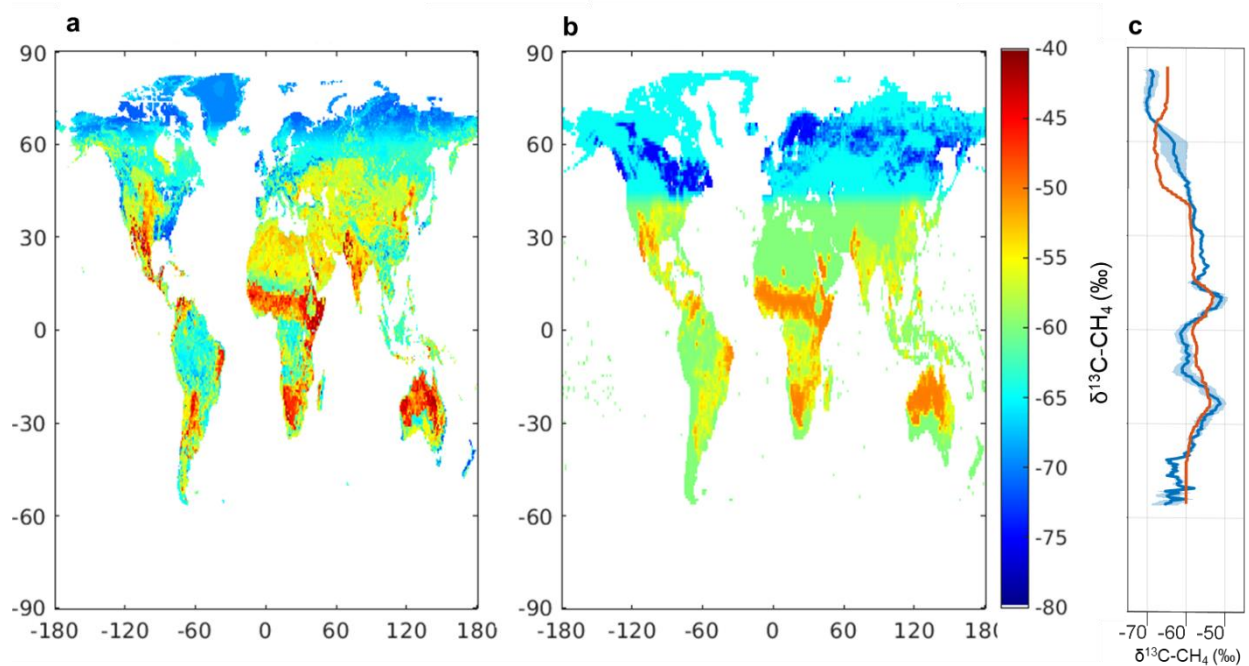
**Supplementary Figure 5. Global soil wetland and vegetation map.** (a) Default wetland type map from Matthews and Fung (1987)<sup>5</sup>, where type 1 and 2 represent forested and non-forested bog, type 3 and 4 represent forested and non-forested swamp, and 5 represents alluvial wetlands. The wetland map was developed based on vegetation, soil properties, and fractional inundation, and it yielded a global distribution of wetland sites identified with in situ ecological and environmental characteristics. (b) Filled wetland type map. For sites without wetland types in panel a, we assigned forested soils for type 1 and non-forested soils for type 2 based on the global vegetation distribution in panel c. (c) Global vegetation distribution<sup>6</sup>, where numbers 1-35 represent ice, alpine tundra & polar desert, wet tundra, boreal forest, forested boreal wetlands, boreal woodlands, non-forested boreal wetlands, mixed temperate forests, temperate coniferous forests, temperate deciduous forests, temperate forested wetlands, tall grasslands, short grasslands, tropical savannas, xeric shrublands, tropical evergreen forests, tropical forested wetlands, tropical deciduous forests, xeric woodlands, tropical forested floodplains, deserts, tropical non-forested wetlands, tropical non-forested floodplains, temperate non-forested wetland, temperate forested floodplains, temperate non-forested floodplains, wet savannas, salt marsh, mangroves, tidal freshwater marshes, temperate savannas, cultivation, temperate evergreen broadleaf, unknown, and mediterranean shrublands, respectively.



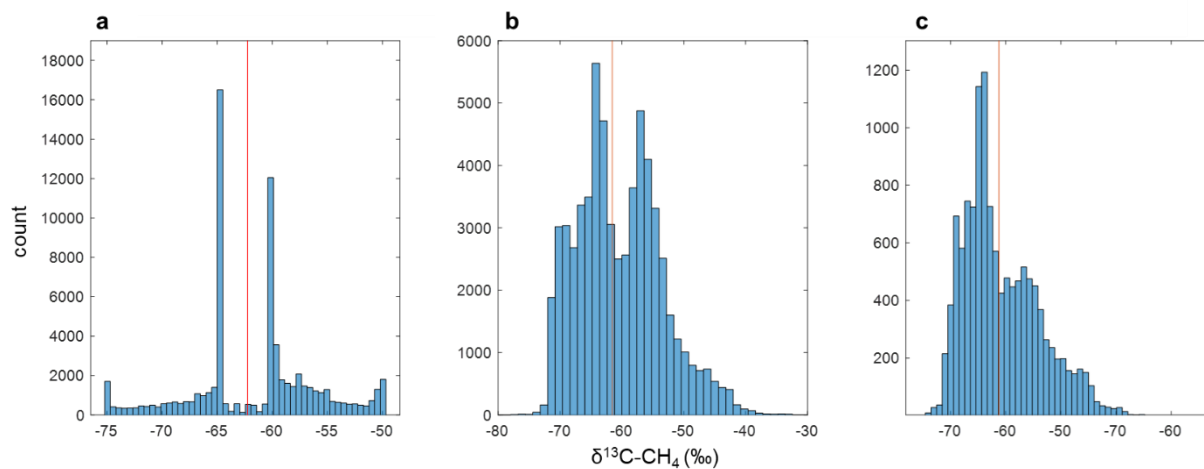
**Supplementary Figure 6. Simulated wetland fluxes with (a) static inundation data from Matthews and Fung (1987)<sup>5</sup> and (b) transient inundation data from Poulter *et al.* (2017)<sup>7</sup>, and (c) their latitudinal sum of fluxes with static (blue) and transient (red) inundation data in 2000.**



**Supplementary Figure 7. Global distribution of wetland  $\delta^{13}\text{C-CH}_4$  and its latitudinal gradients simulated by isoTEM.** (a) Modeled global wetland  $\delta^{13}\text{C-CH}_4$  for wetland grid cells with dynamic inundation data (Poulter et al., 2017<sup>7</sup>). (b) Mean latitudinal distribution of wetland  $\delta^{13}\text{C-CH}_4$ .

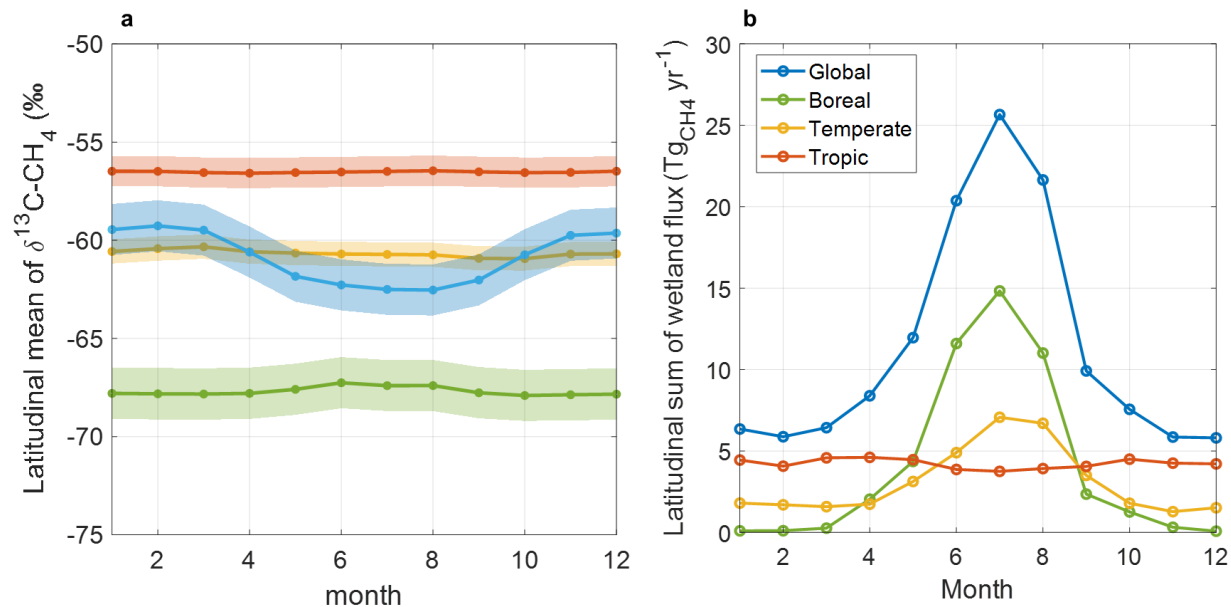


**Supplementary Figure 8.** Global map of wetland  $\delta^{13}\text{C-CH}_4$  by (a) isoTEM in July, 2000 and (b) Ganesan *et al.* (2018)<sup>8</sup>, and (c) their latitudinal mean of  $\delta^{13}\text{C-CH}_4$  by isoTEM (blue) and Ganesan *et al.* (2018)<sup>8</sup> (red). The shaded area represents in panel c one standard deviation determined from 20 ensemble simulations where the optimized parameters were varied.

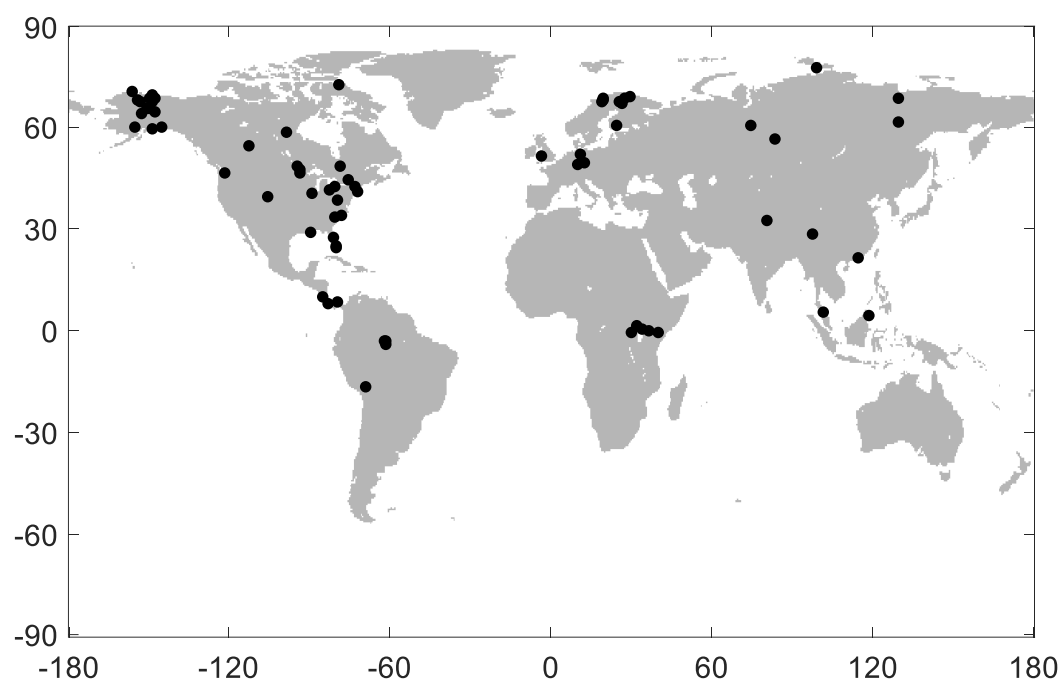


**Supplementary Figure 9. Histograms of modeled global wetland  $\delta^{13}\text{C-CH}_4$  by (a) Ganesan *et al.* (2018)<sup>8</sup>, and isoTEM with (b) all grid cells and (c) wetland cells only. Red lines represent mean of wetland  $\delta^{13}\text{C-CH}_4$ .**

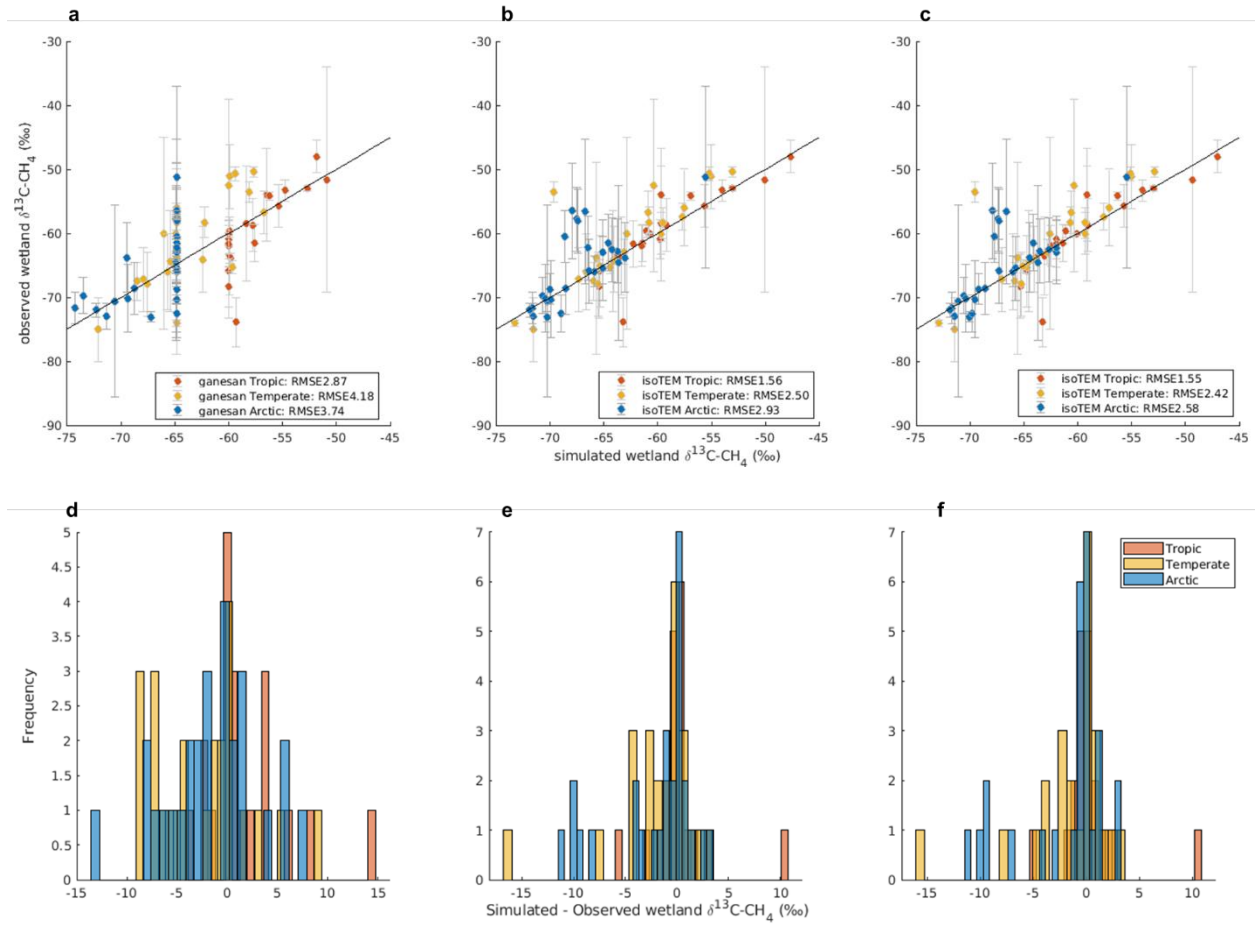




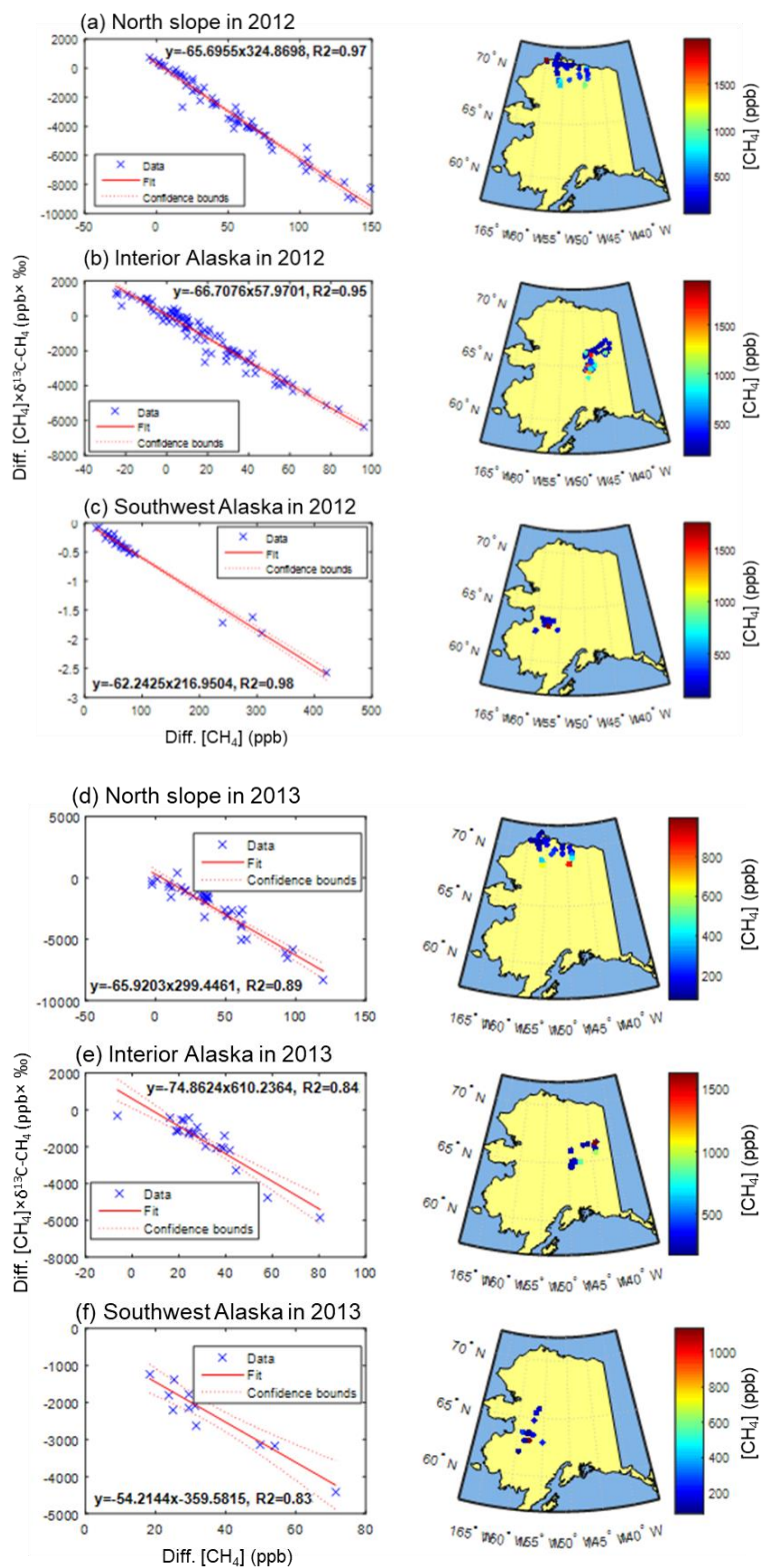
**Supplementary Figure 10. Seasonality of (a) mean  $\delta^{13}\text{C-CH}_4$  and (b) sum of methane fluxes for global (blue), boreal (green), temperate (yellow), and tropic (red) regions with static inundation data<sup>5,9</sup>.** Shaded area in (a) represents one standard deviation by varying the optimized parameters from ensemble simulations. Blue in panel a represents flux-weighted global  $\delta^{13}\text{C-CH}_4$ . At grid and regional scale, the small seasonal variability of  $\delta^{13}\text{C-CH}_4$  has been shown in other literature<sup>10–12</sup>. Studies also pointed out the uncertainty in seasonality of  $\delta^{13}\text{C-CH}_4$ <sup>13</sup>, and the contrasting seasonality for Arctic<sup>12,13</sup>, temperate<sup>11,14</sup>, and tropical wetlands<sup>15,16</sup>.

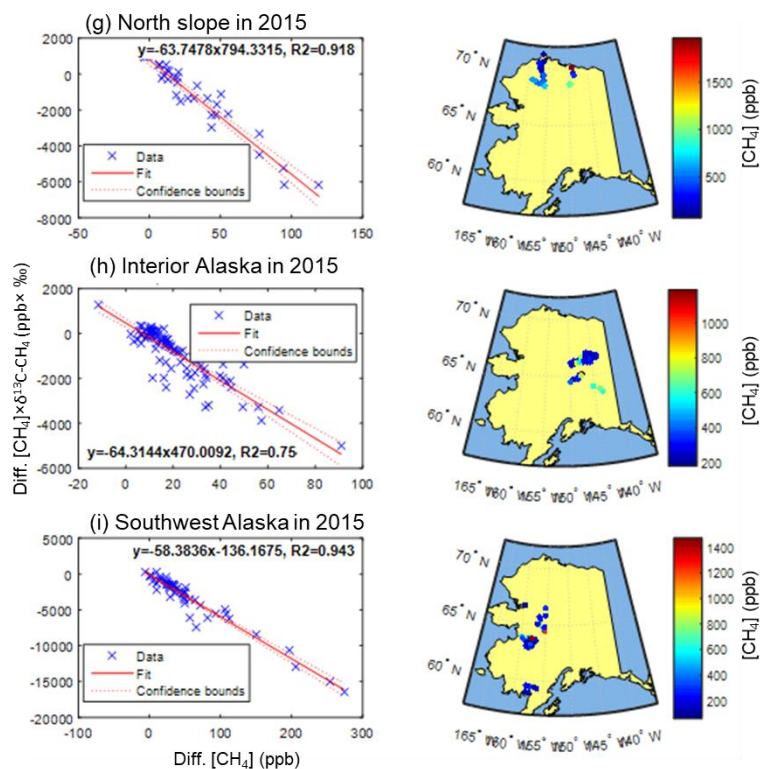


**Supplementary Figure 11. Global map of 70 wetlands sites used for site-level comparison of wetland  $\delta^{13}\text{C-CH}_4$ .** All observation data used for site-level comparison are listed in Supplementary Data 1.

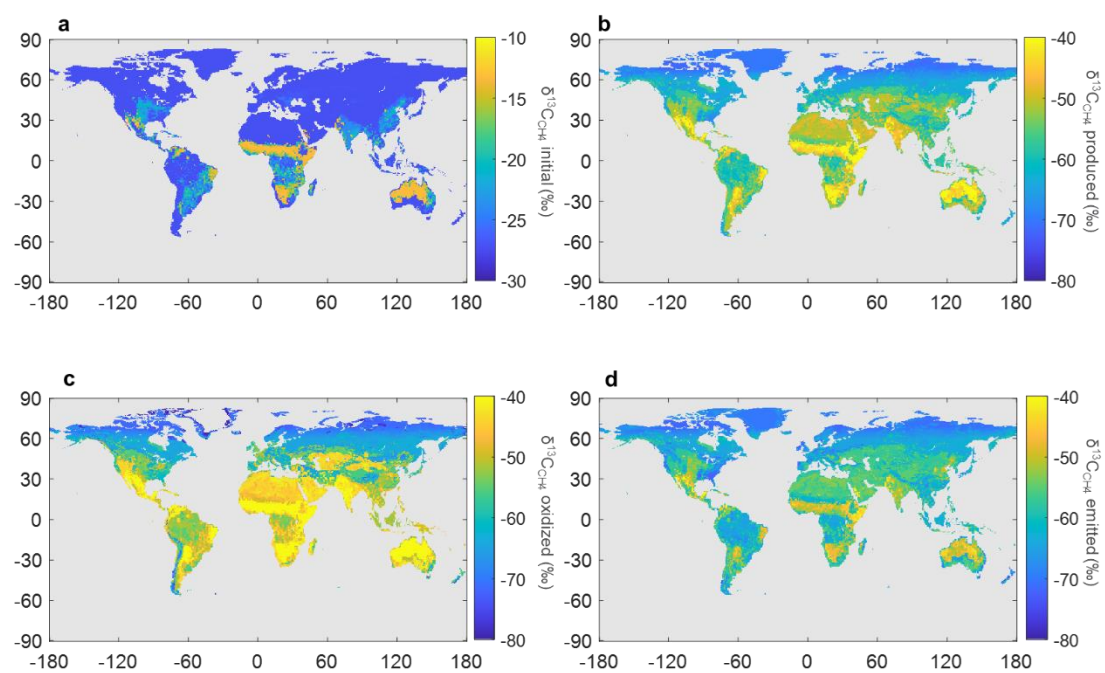


**Supplementary Figure 12. Site-level model-data comparison.** (a-c) Comparison of observations with (a) Ganesan et al. (2018), (b) isoTEM in July 2016, and (c) temporally-varying isoTEM and (d-f) their histograms of the differences between each model and observations from tropic (red), temperate (yellow), and boreal (blue) regions. Error bars in panel a-c represent one standard deviation of measured wetland  $\delta^{13}\text{C-CH}_4$ . All observation data used for site-level comparison are listed in Supplementary Data 1 and Supplementary Figure 11.

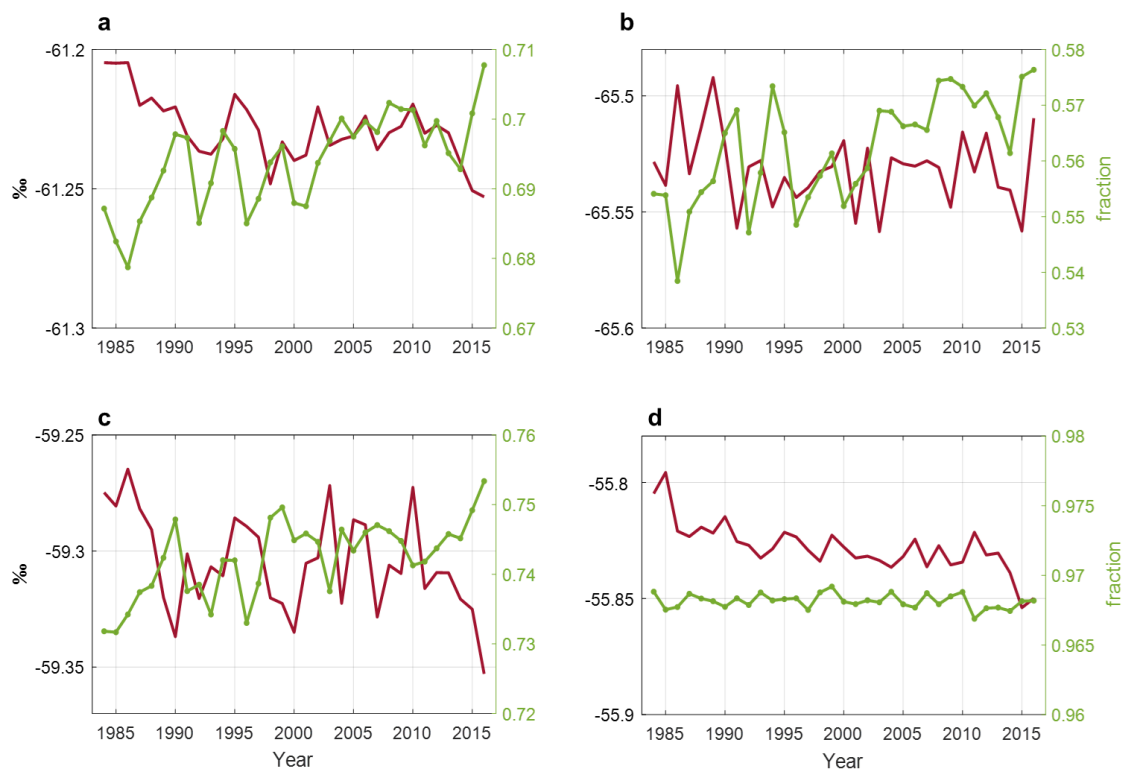




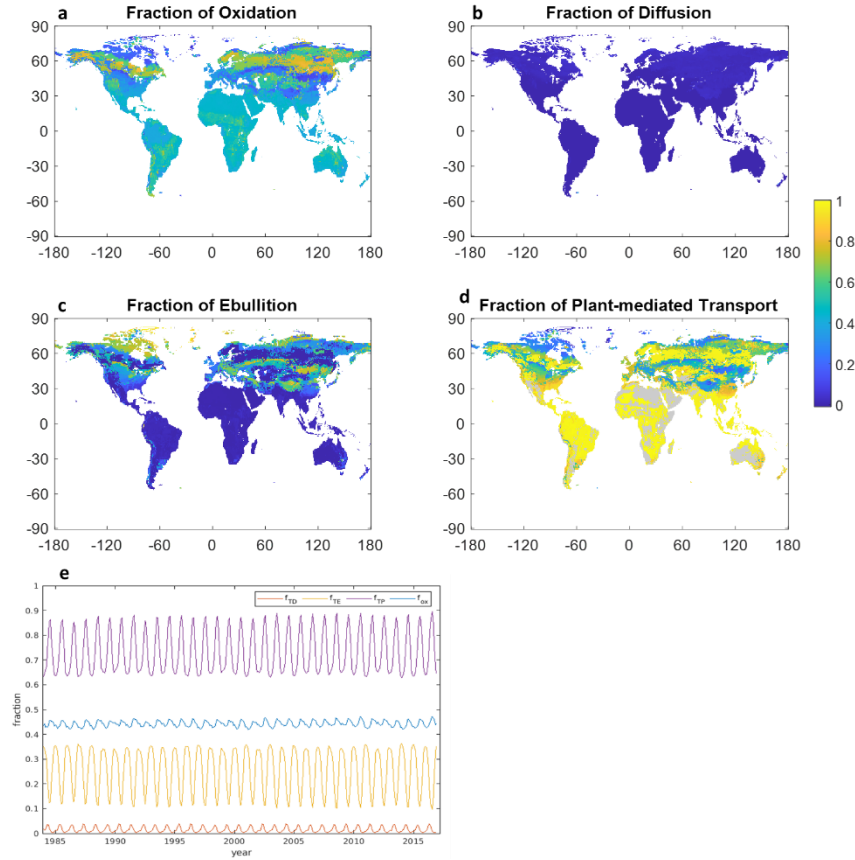
**Supplementary Figure 13. Miller-Tans plots of airborne measurements in (a-c) 2012, (d-f) 2013, and (g-i) 2015 for (a,d,g) North Slope, (b,e,h) interior, and (c,f,i) southwest Alaska.** The left figure of each panel shows curve fitting of Miller-Tans plot<sup>17</sup>, where the slope of the fit represents an estimated source signature of wetland  $\delta^{13}\text{C-CH}_4$ . The right figure of each panel shows data location and  $\text{CH}_4$  mole fraction. The Alaskan maps are generated using a ‘worldmap’ function in Matlab<sup>18</sup>.



**Supplementary Figure 14. Spatial map of  $\delta^{13}\text{C}$  simulated in isoTEM in July, 2000.** Map of  $\delta^{13}\text{C}$  of (a) precursor organic matter, (b) produced  $\text{CH}_4$ , (c) oxidized  $\text{CH}_4$ , and (d)  $\text{CH}_4$  emitted to the soil surface.

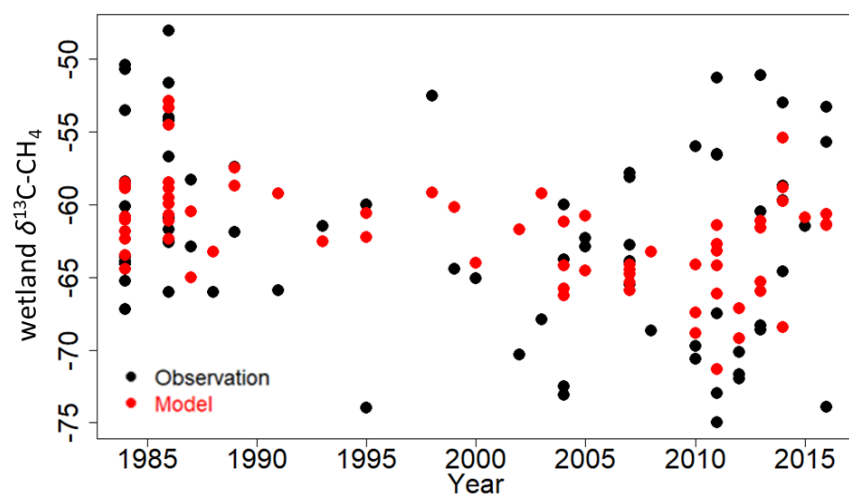


**Supplementary Figure 15. Long-term trends of wetland  $\delta^{13}\text{C}\text{-CH}_4$  simulated without long-term trend of  $\delta^{13}\text{C}_{\text{POM}}$  (maroon), and the fraction of plant-mediated transport over all three transport processes (green) for (a) global scale, (b) boreal, (c) temperate, and (d) tropical regions.**

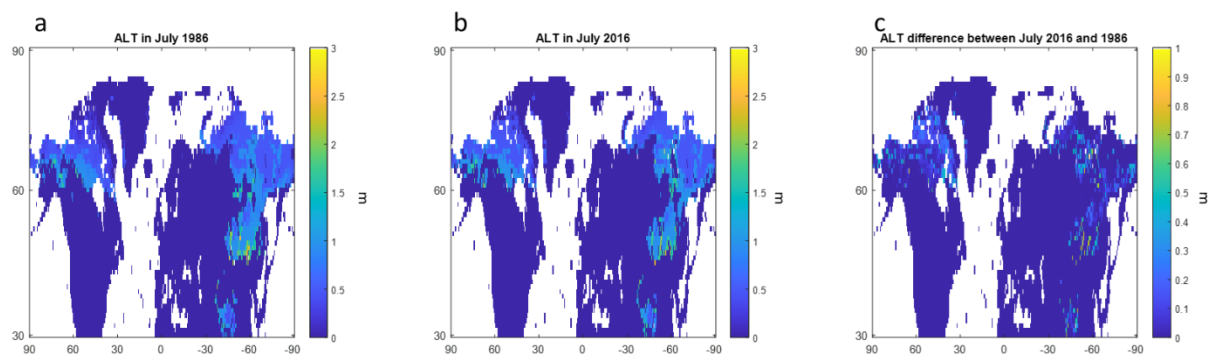


**Supplementary Figure 16. Spatial and temporal variability of the fraction of oxidation, and transport processes.** (a-d) Map of the fraction of (a) oxidation, (b) diffusion, (c) ebullition, and (d) plant-mediated transport. (e) global monthly variability of the fraction of oxidation (blue), diffusion (red), ebullition (yellow), and plant-mediated transport (purple) (Equation 18).

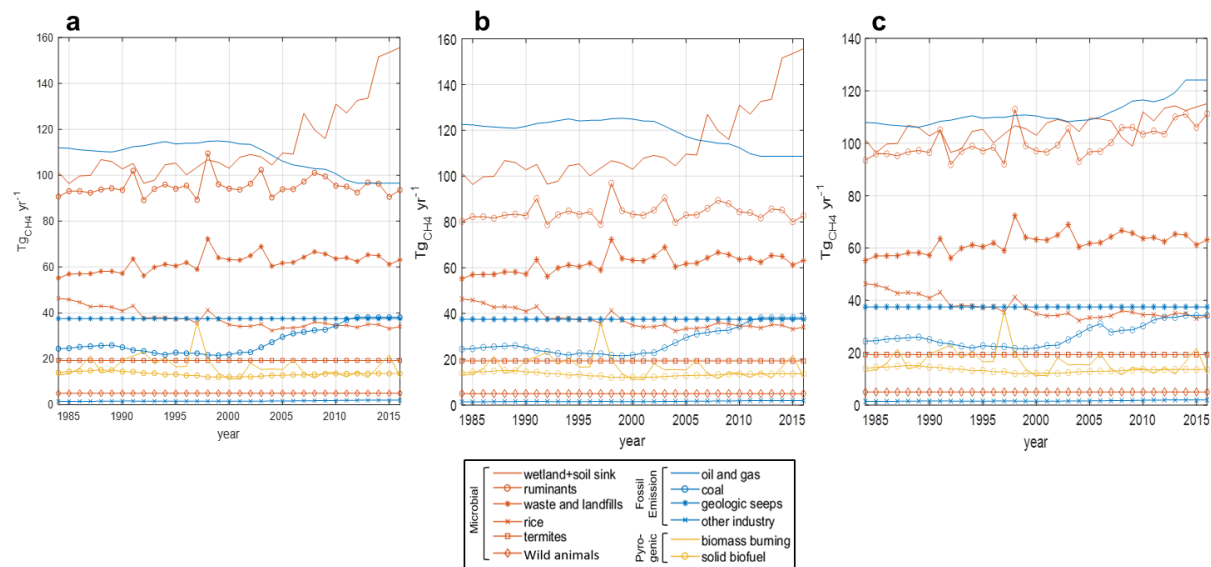




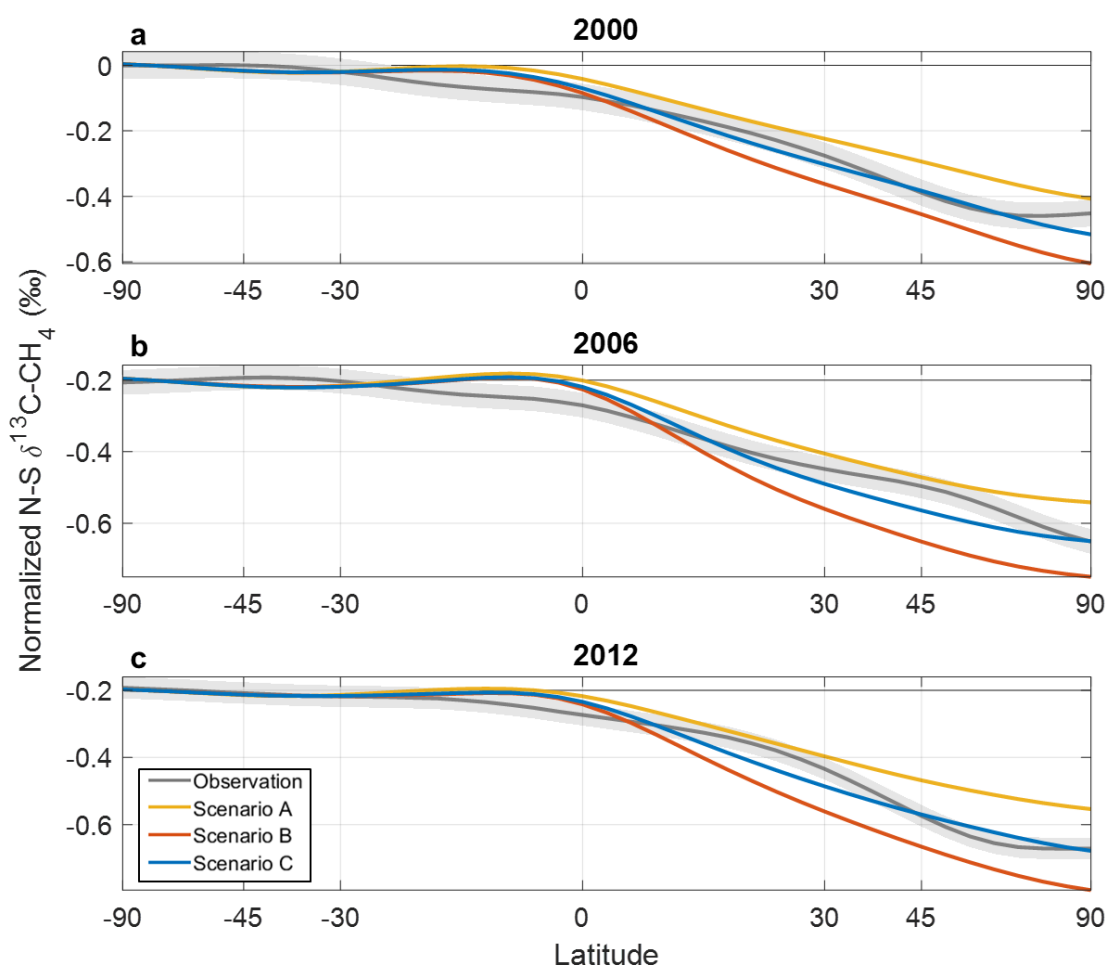
**Supplementary Figure 17. Results of regressions between wetland  $\delta^{13}\text{C-CH}_4$  and year.**



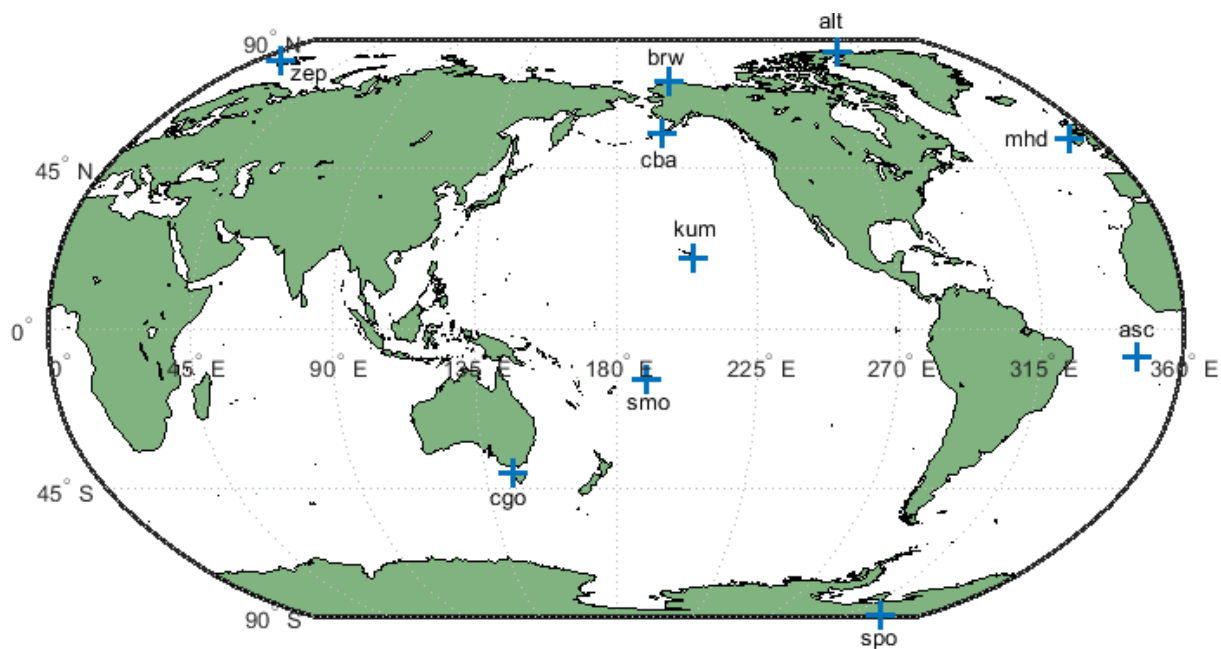
**Supplementary Figure 18. Changes in active layer depth (ALT) simulated by ORCHIDEE-PEAT<sup>19</sup>, under the RCP8.5 scenario. (a) ALT in July 1986, (b) ALT in July 2016, and (c) differences in ALT between July 2016 and July 1986.**



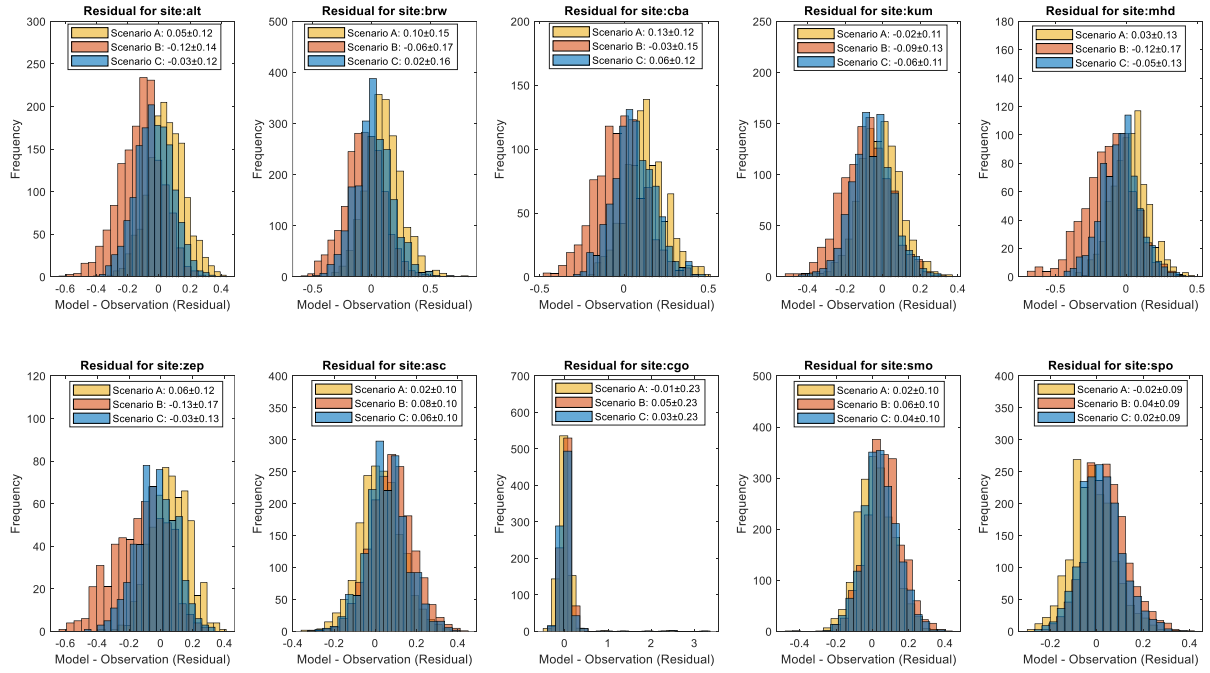
**Supplementary Figure 19. Bottom-up inventory for each source category for Scenarios A-D<sup>5</sup>.** Bottom-up emissions for each category for (a) Scenarios A-B, (b) Scenario C, and (c) Scenario D. The data sources are listed in Supplementary Table 6. Information about Scenarios A-D is in Table 1.



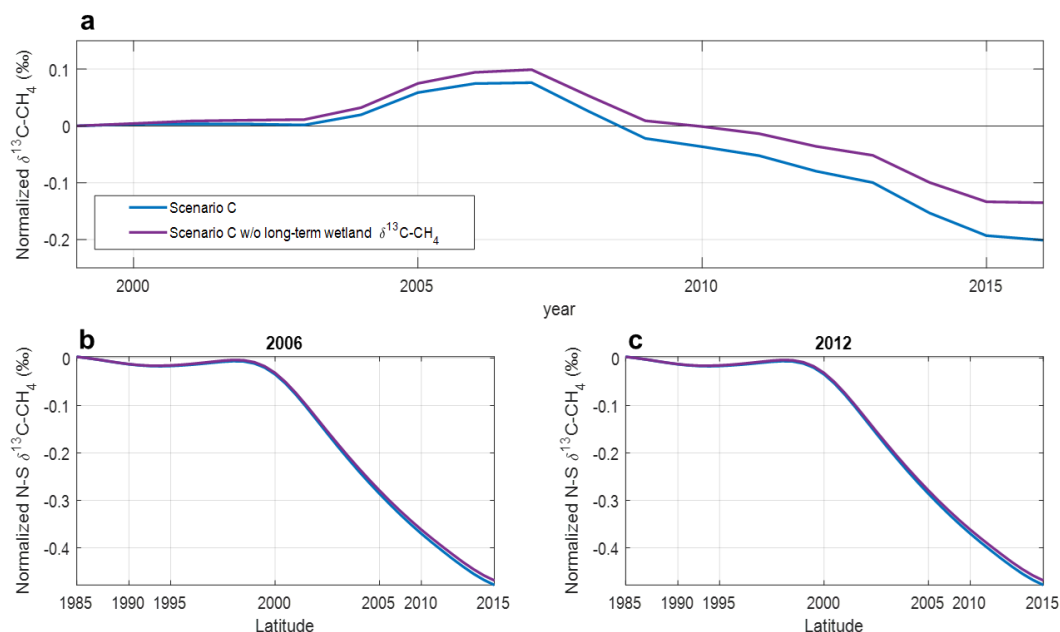
**Supplementary Figure 20. Observed and simulated normalized north-south annual mean gradient of atmospheric  $\delta^{13}\text{C-CH}_4$  for scenarios A-C.** The north-south  $\delta^{13}\text{C-CH}_4$  was calculated by zonally-averaging the surface  $\delta^{13}\text{C-CH}_4$  and normalized based on the  $\delta^{13}\text{C-CH}_4$  at 60-90 °S for (a) 2000, (b), 2006, and (c) 2012. The shaded gray area for observation is formed from 100 data extension and integration surfaces within each of the uncertainty metrics such as network, atmospheric, and bias. The north-south gradient of atmospheric  $\delta^{13}\text{C-CH}_4$  for other years is in Supplementary Table 7. Information about scenarios A-C is in Table 1.



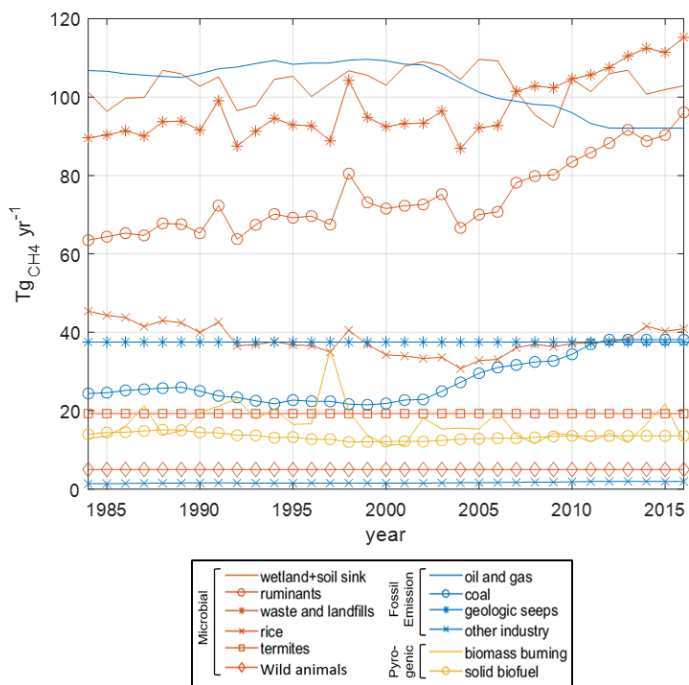
**Supplementary Figure 21. Map of 10 observations sites for atmospheric  $\delta^{13}\text{C}\text{-CH}_4$  measurements.** More information about observation sites is in Supplementary Table 10. The Alaskan maps are generated using a ‘worldmap’ function in Matlab<sup>18</sup>.



**Supplementary Figure 22. Histogram of the differences between simulated and observed  $\delta^{13}\text{C-CH}_4$  (in ‰) for Scenarios A-C.** The observed  $\delta^{13}\text{C-CH}_4$  is from 10 NOAA/INSTAAR surface flask measurement sites during the entire observation period listed in Supplementary Table 8. Information about scenarios A-C is in Table 1.

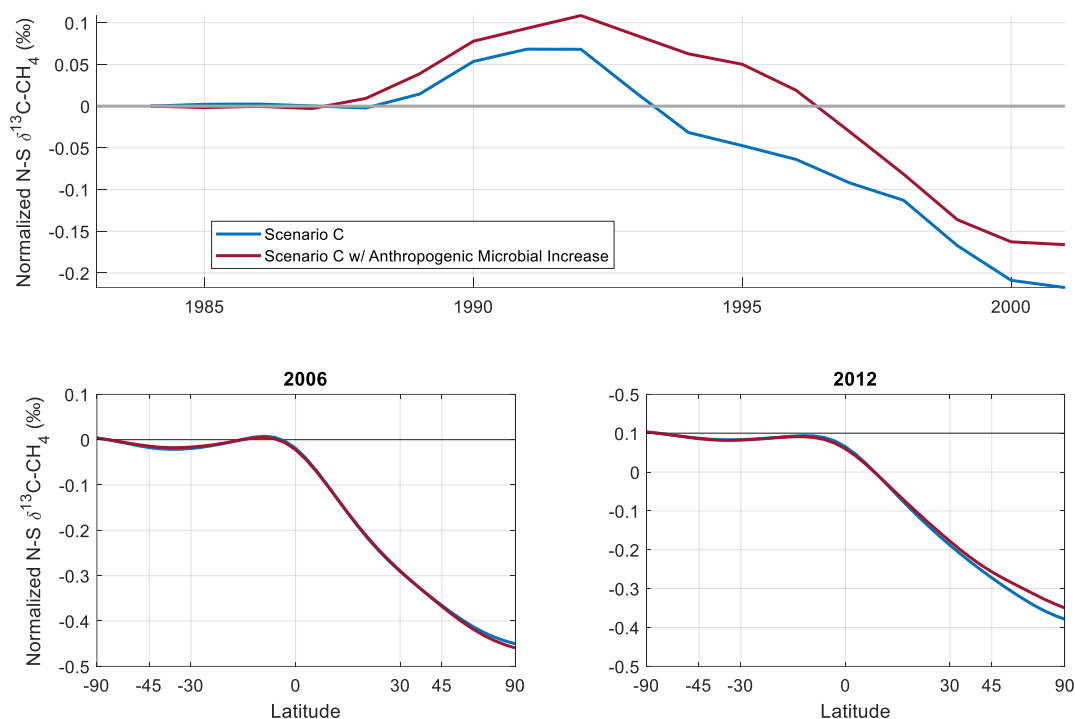


**Supplementary Figure 23. Normalized (a) long-term trend of globally averaged atmospheric  $\delta^{13}\text{C-CH}_4$  and (b-c) north-south annual mean gradient of atmospheric  $\delta^{13}\text{C-CH}_4$ .** Scenario C (blue) is the same in Figure 4 and Table 1, and Scenario C without long-term wetland  $\delta^{13}\text{C-CH}_4$  (purple) removed long-term decrease trend in wetland  $\delta^{13}\text{C-CH}_4$  of  $\sim 0.6\text{‰}$  during 1984-2016. The long-term trend is normalized based on the global mean  $\delta^{13}\text{C-CH}_4$  in 1998, and the north-south gradient is normalized based on the  $\delta^{13}\text{C-CH}_4$  at 60-90 °S for (b) 2006, and (c) 2012.

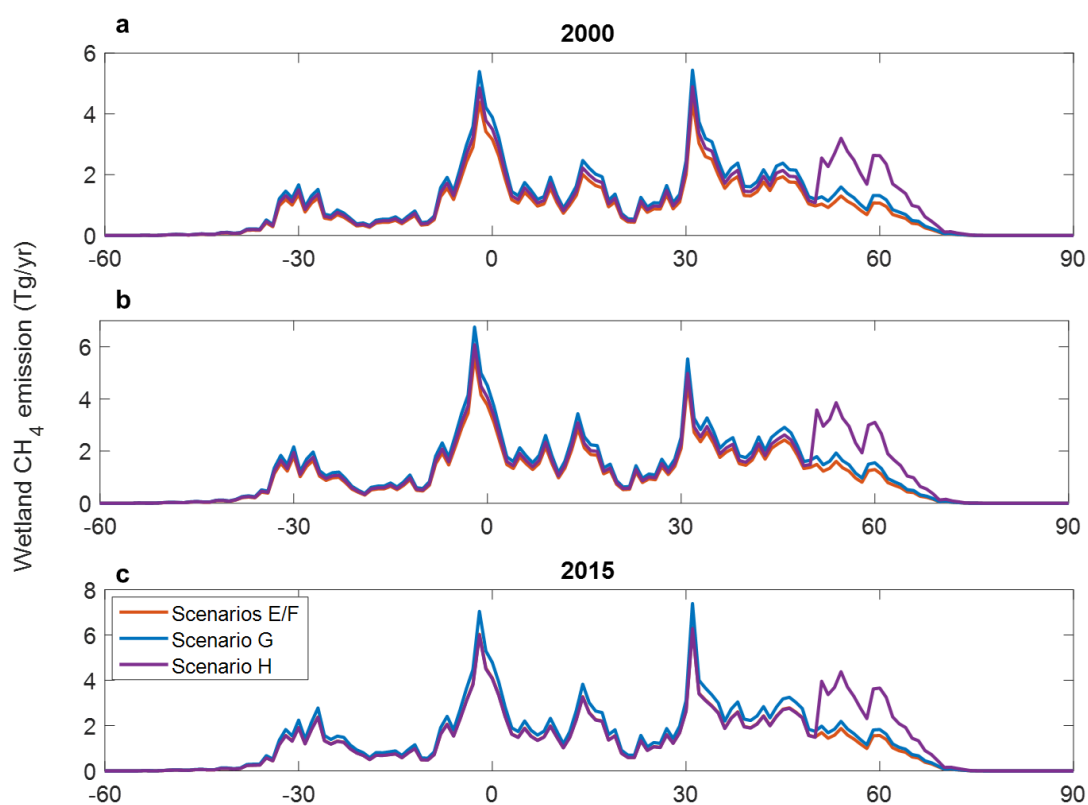


**Supplementary Figure 24. Bottom-up inventory for each source category for Scenario C with anthropogenic microbial increase.** The data sources are listed in Supplementary Table 8.

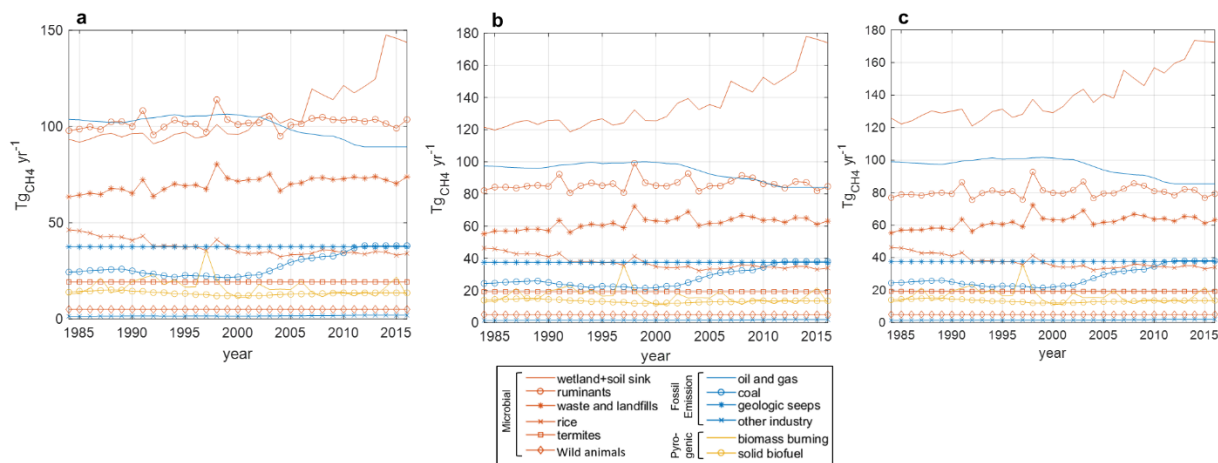




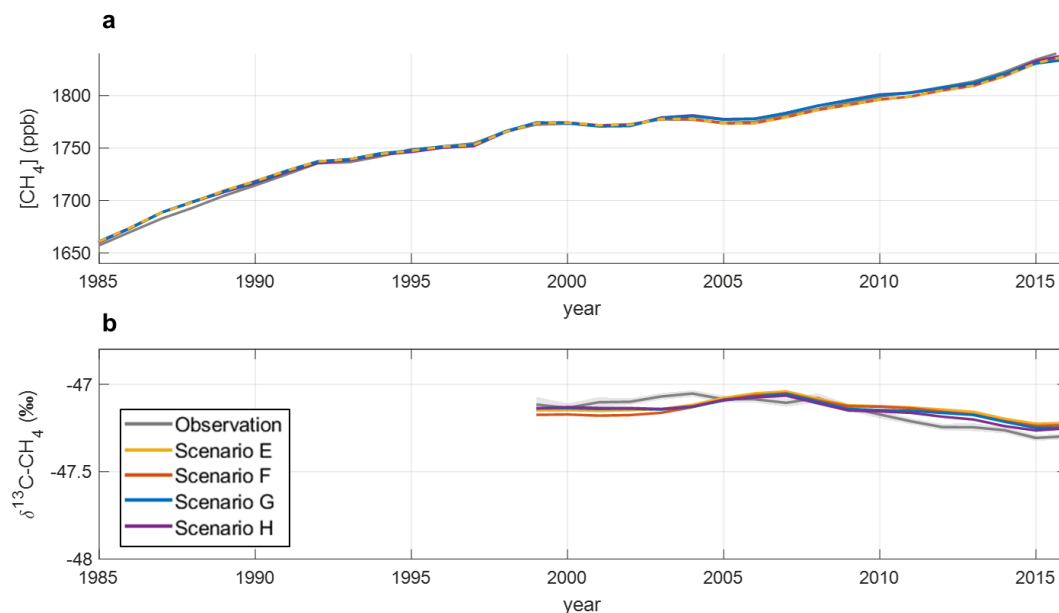
**Supplementary Figure 25. Normalized (a) long-term trend of globally averaged atmospheric  $\delta^{13}\text{C-CH}_4$  and (b-c) north-south annual mean gradient of atmospheric  $\delta^{13}\text{C-CH}_4$ .** Scenario C (blue) is the same in Figure 4 and Table 1, and the annual emission setup of Scenario C with anthropogenic microbial increase (maroon) during 1984-2016 is in Supplementary Figure 24. The long-term trend is normalized based on the global mean  $\delta^{13}\text{C-CH}_4$  in 1998, and the north-south gradient is normalized based on the  $\delta^{13}\text{C-CH}_4$  at 60-90 °S for (b) 2006, and (c) 2012.



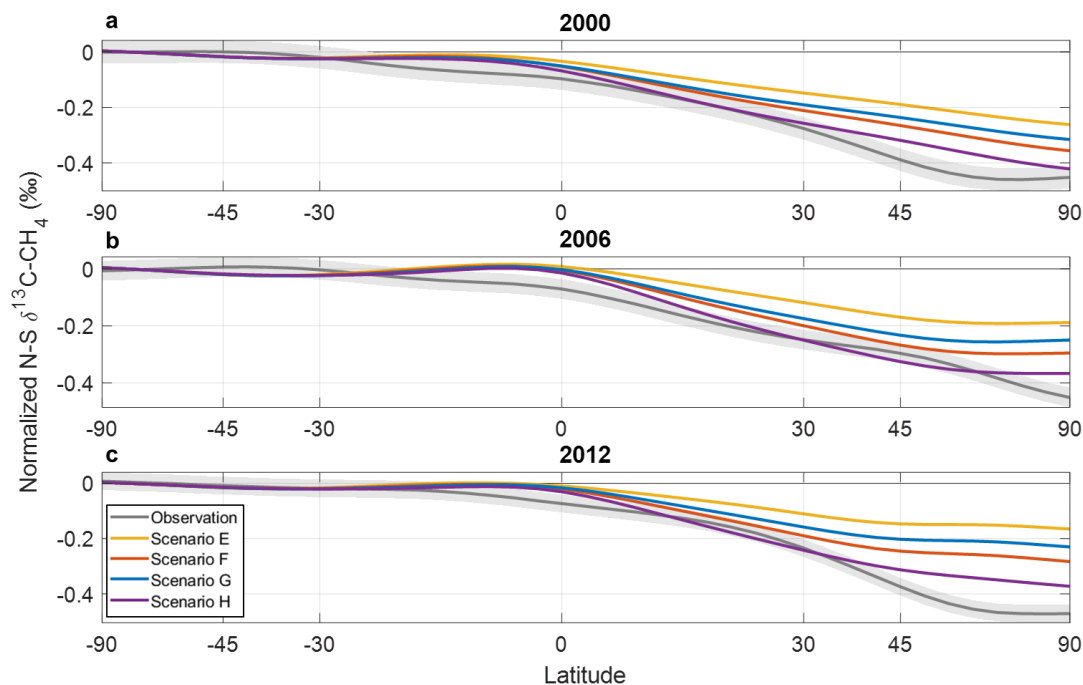
**Supplementary Figure 26. Latitudinal gradients of wetland CH<sub>4</sub> emission for scenarios E-H with transient inundation data<sup>7</sup>.** Latitudinal gradients of total wetland CH<sub>4</sub> emissions for scenarios E/F (red), G (blue), and H (purple) for (a) 2000, (b) 2010, and (c) 2015. Information about scenarios E-H is in Supplementary Table 11.



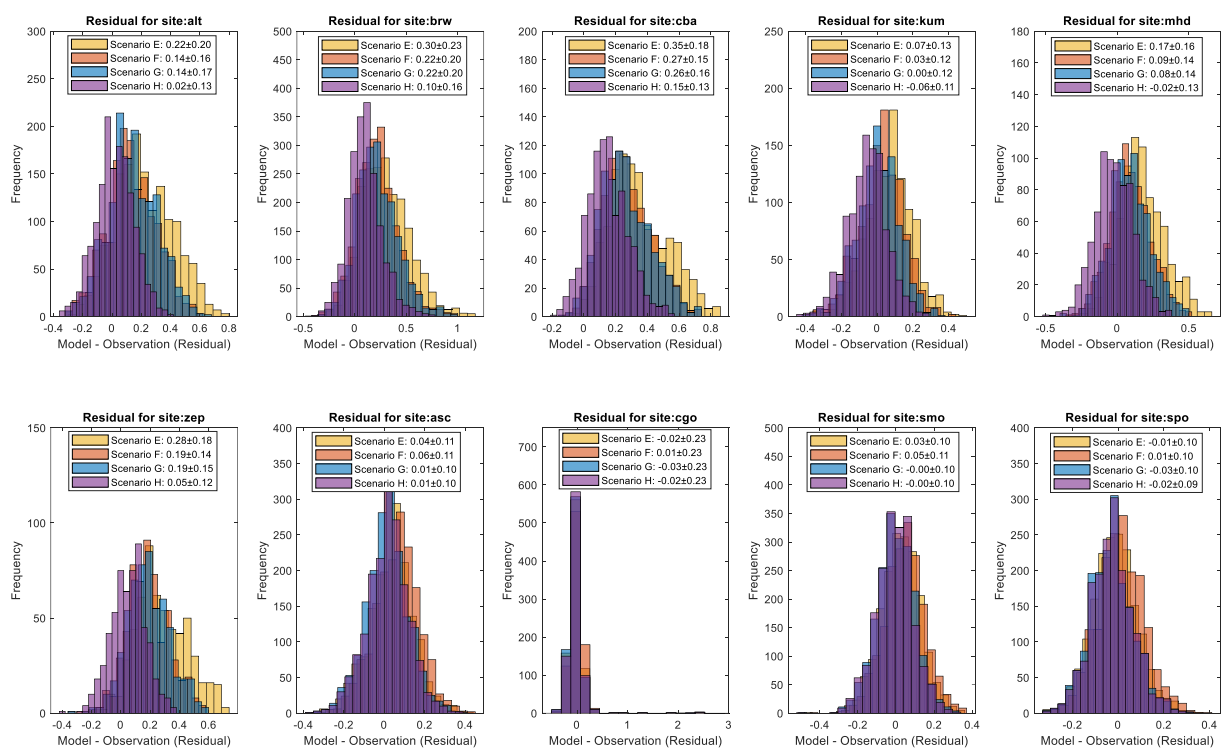
**Supplementary Figure 27. Bottom-up inventory for each category for Scenarios E-H with transient inundation data<sup>7</sup>.** Bottom-up emissions for each category for (a) Scenario E/F, (b) Scenario G, and (c) Scenario H with transient inundation data from Poulter et al. (2017)<sup>7</sup>. The data sources are listed in Supplementary Table 7 and the scenario information is listed in Supplementary Table 11.



**Supplementary Figure 28. Long-term trend of globally averaged atmospheric  $\text{CH}_4$  and  $\delta^{13}\text{C-CH}_4$  for Scenarios E-H.** Model-data comparison of long-term trend of atmospheric  $\text{CH}_4$  (in ppb) and  $\delta^{13}\text{C-CH}_4$  (in ‰) by observation (grey) and simulations from Scenario E (yellow), F (red), G (blue), and H (purple) with transient inundation from Poulter et al. (2017)<sup>7</sup>. The shaded gray area for observation is formed from 100 data extension and integration surfaces within each of the uncertainty metrics such as network, atmospheric, and bias. Information about scenarios E-H are in Supplementary Table 11.



**Supplementary Figure 29. Observed and simulated normalized north-south annual mean gradient of atmospheric  $\delta^{13}\text{C-CH}_4$  for scenarios E-H.** The north-south  $\delta^{13}\text{C-CH}_4$  was calculated by zonally-averaging the observed and simulated surface  $\delta^{13}\text{C-CH}_4$  and normalized based on the  $\delta^{13}\text{C-CH}_4$  at 60-90 °S for (a) 2000, (b) 2006, and (c) 2012 for Scenario E (yellow), F (red), G (blue), and H (purple). The shaded gray area for observation is formed from 100 data extension and integration surfaces within each of the uncertainty metrics such as network, atmospheric, and bias. Information about scenarios E-H are in Supplementary Table 11.



**Supplementary Figure 30. Histogram of the differences between simulated and observed  $\delta^{13}\text{C-CH}_4$  for Scenarios E-H.** The observed  $\delta^{13}\text{C-CH}_4$  is from 10 NOAA/INSTAAR surface flask measurement sites during the entire observation period listed in Supplementary Table 8. Information about scenarios E-H is in Supplementary Table 11.

## **Supplementary Table Captions**

**Supplementary Table 1. Coefficients for a multiple regression of the fractional contribution of methanogenic community.**

**Supplementary Table 2. Information about observation sites for model optimization.**

**Supplementary Table 3. Upper and lower limits of parameter range of fractionation factors ( $\alpha$ ), where AM=acetoclastic methanogenesis, HM=hydrogenotrophic methanogenesis, MO=methane oxidation, TP=plant-mediated transport.**

**Supplementary Table 4. Optimized Parameters related to methane fractionation factors in wetlands.**

**Supplementary Table 5. Regional-level observations from airborne measurements for three regions in Alaska during 2012-2013, and 2015 using Miller-Tans plots.**

**Supplementary Table 6. Coefficients of a multiple regression of the wetland  $\delta^{13}\text{C-CH}_4$ .**

**Supplementary Table 7. Model Sensitivity test using meteorological inputs and wetland inundation data.**

**Supplementary Table 8. Data sources for total emissions and  $\delta^{13}\text{C-CH}_4$  source signatures for atmospheric modeling. More information in Lan et al. (2021)<sup>22</sup>.**

**Supplementary Table 9. Observed and simulated normalized north-south annual mean gradient of atmospheric  $\delta^{13}\text{C-CH}_4$  for scenarios A-C during 2000-2016. The north-south gradient was calculated as the difference of  $\delta^{13}\text{C-CH}_4$  between 60-90 °S and 60-90 °N.**

**Supplementary Table 10. Information on measurement sites for atmospheric  $\delta^{13}\text{C}$ -CH<sub>4</sub>.**

**Supplementary Table 11. Setup of TM5 atmospheric modeling for Scenarios E-H.**



## Supplementary Tables

**Supplementary Table 1. Coefficients for a multiple regression of the fractional contribution of methanogenic community.**

	<b>a<sub>1</sub></b>	<b>a<sub>2</sub></b>	<b>b</b>	<b>c</b>	<b>d</b>
<b>Parameter</b>	Latitudinal gradient	Latitudinal gradient for > 60 °N	pH gradient	SOC gradient	Intercept
<b>Value</b>	0.11±0.02	5.19±0.10	-9.23±0.15	-0.70±0.06	102.93±1.62
<b>Significance</b> (p-value)		* 0.05	* 0.05		* 0.05

**Supplementary Table 2. Information about observation sites for model optimization.**

<b>Vegetation Types</b>	<b>Lat, Lon</b>	<b>Meteorological Inputs</b>	<b>Observation Data</b>	<b>References</b>
Boreal wetlands	68, 18.5	Site observed temperature and precipitation and CRU	CH <sub>4</sub> flux and $\delta^{13}\text{C}$ -CH <sub>4</sub> in 2012-2013	McCalley <i>et al.</i> , 2014 <sup>10</sup> Deng et al. 2017 <sup>23</sup>
Temperate wetlands	48, -95	Site observed temperature and CRU	CH <sub>4</sub> flux and $\delta^{13}\text{C}$ -CH <sub>4</sub> in 1989-1990	Kelly <i>et al.</i> , 1992 <sup>11</sup>
Tropical wetlands	27.5, -82.5	Site observed temperature and CRU	CH <sub>4</sub> flux in 1986-1987	Burke, Barber and Sackett, 1988, 1992 <sup>24,25</sup>

**Supplementary Table 3. Upper and lower limits of parameter range of fractionation factors ( $\alpha$ ), where AM=acetoclastic methanogenesis, HM=hydrogenotrophic methanogenesis, MO=methane oxidation, TP=plant-mediated transport.**

	Lower Bound	Upper Bound	Literature
$\alpha_{AM}$	1.000	1.040	Conrad et al., 2005; Vaughn et al., 2016; Conrad et al., 2010 <sup>16,26,27</sup>
$\alpha_{HM}$	1.030	1.080	Conrad et al., 2005; Vaughn et al., 2016; Conrad et al., 2010 <sup>16,26,27</sup>
$\alpha_{MO}$	1.015	1.035	King, 1989; Chanton, 2005; Zhang et al., 2016 <sup>28–30</sup>
$\alpha_{TP}$	1.000	1.030	Chanton, 2005 <sup>29</sup>

**Supplementary Table 4. Optimized Parameters related to methane fractionation factors in wetlands.**

Region	Wetland Type	$\alpha_{AM}$	$\alpha_{HM}$	$\alpha_{MO}$	$\alpha_{TP}$
Boreal	Forested	1.0238 $\pm 0.0087$	1.0456 $\pm 0.0004$	1.0151 $\pm 0.0002$	1.0151 $\pm 0.0002$
	Non-forested	1.0242 $\pm 0.0065$	1.0428 $\pm 0.0017$	1.0151 $\pm 0.0002$	1.0142 $\pm 0.0003$
Temperate	Forested	1.0135 $\pm 0.0078$	1.0648 $\pm 0.0074$	1.0168 $\pm 0.0026$	1.0298 $\pm 0.0003$
	Non-forested	1.0186 $\pm 0.0051$	1.0533 $\pm 0.0057$	1.0190 $\pm 0.0013$	1.0256 $\pm 0.0013$
Tropic	Forested	1.0111 $\pm 0.0065$	1.0480 $\pm 0.0101$	1.0164 $\pm 0.0018$	1.0281 $\pm 0.0026$
	Non-forested	1.0106 $\pm 0.0052$	1.0553 $\pm 0.0139$	1.0155 $\pm 0.0008$	1.0292 $\pm 0.0013$
Average		1.0170 $\pm 0.0061$	1.0517 $\pm 0.0080$	1.0163 $\pm 0.0015$	0.0237 $\pm 0.0071$

**Supplementary Table 5. Regional-level observations from airborne measurements for three regions in Alaska during 2012-2013, and 2015 using Miller-Tans plots.**

	Slope of Miller-Tans plot (wetland $\delta^{13}\text{C-CH}_4$ ) (‰)		
<b>Year</b>	<b>North Slope</b>	<b>Interior Alaska</b>	<b>Southwest Alaska</b>
<b>2012</b>	-65.90	-66.43	-62.61
<b>2013</b>	-65.92	-75.47	-54.67
<b>2015</b>	-63.65	-64.31	-59.74
<b>Mean</b>	-65.16	-68.74	-59.01
<b>Standard Deviation</b>	1.30	5.93	4.02

**Supplementary Table 6. Coefficients of a multiple regression of the wetland  $\delta^{13}\text{C}\text{-CH}_4$ .**

	<b>a</b>	<b>b</b>	<b>c</b>	<b>d</b>	<b>e</b>
<b>Parameter</b>	Latitudinal gradient	pH gradient	SOC gradient	Year gradient	Intercept
<b>Value</b>	-0.10	2.21	-0.20	-0.11	152.85
<b>Significance (p-value)</b>	* 0.001	* 0.01		* 0.1	* 0.05

**Supplementary Table 7. Model Sensitivity test using meteorological inputs and wetland inundation data.**

<b>Mean <math>\delta^{13}\text{C}</math>-CH<sub>4</sub> (‰)</b>	<b>Arctic</b>	<b>Temperate</b>	<b>Tropic</b>	<b>Global</b>
<b>Default (without long-term trend in <math>\delta^{13}\text{C}</math>-POM)</b>	<b>-64.54</b>	<b>-58.46</b>	<b>-55.47</b>	<b>-61.04</b>
<b>Air T +3°C</b>	-64.48	-58.36	-55.53	-61.02
<b>Air T -3°C</b>	-64.39	-58.60	-55.39	-60.94
<b>Precipitation +30%</b>	-64.56	-58.46	-55.27	-60.99
<b>Precipitation -30%</b>	-64.54	-58.46	-55.73	-61.13
<b>NPP +30%</b>	-64.53	-58.44	-55.44	-61.03
<b>NPP -30%</b>	-64.54	-58.48	-55.50	-61.06
<b>CH<sub>4</sub> +30%</b>	-64.54	-58.55	-55.68	-61.13
<b>CH<sub>4</sub> -30%</b>	-64.52	-58.39	-55.25	-60.95
<b>Transient Inundation</b>	-65.24	-59.16	-55.43	-61.04
<b>f<sub>HM</sub> uncertainty</b>	-64.90 ~ -64.17	-59.05 ~ -57.87	-55.85 ~ -55.08	-61.45 ~ -60.63

**Supplementary Table 8. Data sources for total emissions and  $\delta^{13}\text{C}$ -CH<sub>4</sub> source signatures for atmospheric modeling. More information in Lan et al. (2021)<sup>22</sup>.**

Source	Source sector	Total emissions	$\delta^{13}\text{C}$ -CH <sub>4</sub> source signatures
<b>Fossil Emission</b>	Coal, oil and natural gas, and other energy/industry	EDGAR 4.3.2 (Janssens-Maenhout et al., 2017) <sup>31</sup> .  Long-term mean emissions adjusted for different scenarios based on the mass balance.	Sherwood et al. (2017) <sup>20</sup>
	Geological seeps	Etiopie et al. (2019) <sup>32</sup>	Etiopie et al. (2019) <sup>32</sup>
<b>Biomass and biofuel burning</b>	Biomass burning fluxes	Reanalysis of the Tropospheric chemical composition project before 1997 (Schultz et al., 2008). GFED 4.1s during 1997-2016 (Van der Werf et al., 2017) <sup>53</sup>	Randerson et al. (2012) <sup>54</sup> and Still et al. (2003) <sup>1</sup>
	Biofuel fluxes	EDGAR 4.3.2	Randerson et al. (2012) <sup>54</sup> and Still et al. (2003) <sup>1</sup>
<b>Microbial Emission</b>	Ruminants fluxes	EDGAR 4.3.2  Long-term mean emissions adjusted for different scenarios based on the mass balance.	Randerson et al. (2012) <sup>54</sup> and Still et al. (2003) <sup>1</sup>
	Waste and landfills fluxes	EDGAR 4.3.2	Sherwood et al. (2017) <sup>20</sup>
	Rice fluxes	EDGAR 4.3.2	Sherwood et al. (2017) <sup>20</sup>



	Wild animals and termites fluxes	Bergamaschi et al. (2007) <sup>34</sup>	Sherwood et al. (2017) <sup>20</sup>
	Wetland and soil sink	Based on Liu et al. (2020) <sup>9</sup> and static and transient inundation data <sup>5,7</sup> .  Emission varied based on scenario setup.	isoTEM simulation results (this study) and Ganesan et al. (2018) <sup>8</sup>

**Supplementary Table 9. Observed and simulated normalized north-south annual mean gradient of atmospheric  $\delta^{13}\text{C-CH}_4$  for scenarios A-C during 2000-2016. The north-south gradient was calculated as the difference of  $\delta^{13}\text{C-CH}_4$  between 60-90 °S and 60-90 °N.**

	<b>Observation</b>	<b>Scenario A</b>	<b>Scenario B</b>	<b>Scenario C</b>
<b>2000</b>	0.46±0.04	0.39	0.59	0.50
<b>2001</b>	0.49±0.05	0.40	0.61	0.51
<b>2002</b>	0.41±0.03	0.37	0.57	0.48
<b>2003</b>	0.45±0.03	0.37	0.58	0.48
<b>2004</b>	0.44±0.03	0.33	0.53	0.43
<b>2005</b>	0.53±0.04	0.32	0.51	0.42
<b>2006</b>	0.43±0.03	0.34	0.54	0.44
<b>2007</b>	0.48±0.04	0.40	0.62	0.51
<b>2008</b>	0.36±0.05	0.38	0.59	0.49
<b>2009</b>	0.47±0.03	0.33	0.54	0.44
<b>2010</b>	0.44±0.04	0.35	0.58	0.47
<b>2011</b>	0.43±0.03	0.36	0.59	0.48
<b>2012</b>	0.48±0.03	0.34	0.58	0.47
<b>2013</b>	0.43±0.04	0.33	0.56	0.45
<b>2014</b>	0.40±0.03	0.33	0.58	0.47
<b>2015</b>	0.42±0.03	0.35	0.61	0.48
<b>2016</b>	0.53±0.03	0.35	0.61	0.49
<b>mean</b>	0.45±0.05	0.36±0.03	0.58±0.03	0.47±0.03

**Supplementary Table 10. Information on measurement sites for atmospheric  $\delta^{13}\text{C}$ -CH<sub>4</sub>.**

	<b>Code</b>	<b>Name</b>	<b>Country</b>	<b>Latitude</b>	<b>Longitude</b>	<b>Elevation (meters)</b>	<b><math>\delta^{13}\text{C}</math>-CH<sub>4</sub> data</b>
<b>1</b>	ASC	Ascension Island	United Kingdom	-7.97	-14.40	85	1998-2016
<b>2</b>	ALT	Alert, Nunavut	Canada	82.45	-62.51	185	1998-2016
<b>3</b>	BRW	Barrow Atmospheric Baseline Observatory	United States	71.32	-156.61	11	1998-2016
<b>4</b>	CBA	Cold Bay, Alaska	United States	55.21	-162.72	21.3	2009-2016
<b>5</b>	CGO	Cape Grim, Tasmania	Australia	-40.68	144.69	94	1998-2016
<b>6</b>	KUM	Cape Kumukahi, Hawaii	United States	19.74	-155.01	0.3	1998-2016
<b>7</b>	MHD	Mace Head, County Galway	Ireland	53.33	-9.90	5	1998-2016
<b>8</b>	SMO	Tutuila	American Samoa	-14.25	-170.56	42	1998-2016
<b>9</b>	SPO	South Pole, Antarctica	United States	-89.98	-24.80	2810	1998-2016
<b>10</b>	ZEP	Ny-Alesund, Svalbard	Norway and Sweden	78.91	11.89	474	2008-2016

**Supplementary Table 11. Setup of TM5 atmospheric modeling for Scenarios E-H.**

\*Using an isotope mass balance model from previous studies<sup>22</sup>, the long-term mean fossil and ruminant fluxes were adjusted to match the simulated growth rate of CH<sub>4</sub> during 1984-2016 and the 1998-2016 mean of  $\delta^{13}\text{C-CH}_4$  with observation. By conducting the mass balance for all scenarios, we intended to reduce the spin-up time for atmospheric  $\delta^{13}\text{C-CH}_4$  to be stabilized and compare all scenarios fairly (Method 6a).

Scenario	Wetland isotope map	Assumption of post-2007 CH <sub>4</sub> increase	Global mass balance of CH <sub>4</sub> and $\delta^{13}\text{C-CH}_4^*$
<b>E: Uniform w/ Microbial Increase + transient inundation</b>	One uniform value (-62.3‰, a mean signature of Ganesan <sup>8</sup> )	Wetland emission increase  (46 Tg/yr increase from 1999-2006 to 2016)	Yes
<b>F: Ganesan w/ Microbial Increase + transient inundation</b>	Static Spatially resolved map from Ganesan et al. (2018) <sup>8</sup> (mean of -62.3 ‰)		
<b>G: isoTEM w/ Microbial Increase + transient inundation</b>	Spatio-temporally resolved maps from isoTEM (mean of -61.3 ‰)  (this study)		
<b>H: isoTEM w/ Boreal microbial Increase + transient inundation</b>		Wetland emission is set to be 2.5 times larger in the boreal region  (50-90 °N) (Fig. S20)	

## References

1. Still, C. J., Berry, J. A., Collatz, G. J. & DeFries, R. S. Global distribution of C<sub>3</sub> and C<sub>4</sub> vegetation: Carbon cycle implications. *Global Biogeochem. Cycles* **17**, 6-1-6-14 (2003).
2. Graven, H. *et al.* Compiled records of carbon isotopes in atmospheric CO<sub>2</sub> for historical simulations in CMIP6. *Geosci. Model Dev.* **10**, 4405–4417 (2017).
3. Lassey, K. R., Etheridge, D. M., Lowe, D. C., Smith, A. M. & Ferretti, D. F. Centennial evolution of the atmospheric methane budget: What do the carbon isotopes tell us? *Atmos. Chem. Phys.* **7**, 2119–2139 (2007).
4. Wieder, W. R., Boehnert, J., Bonan, G. B. & Langseth, M. RegridDED harmonized world soil database v1. 2. *ORNL DAAC* (2014).
5. Matthews, E., and Fung, I. Methane emission from natural wetlands: Global distribution, area, and environmental characteristics of sources. *Global Biogeochem. Cycles* **1**, 61–86 (1987).
6. Melillo, J. M. *et al.* Global climate change and terrestrial net primary production. *Nature* **363**, 234 (1993).
7. Poulter, B. *et al.* Global wetland contribution to 2000 – 2012 atmospheric methane growth rate dynamics. *Environ. Res. Lett.* **12**, (2017).
8. Ganesan, A. L. *et al.* Spatially Resolved Isotopic Source Signatures of Wetland Methane Emissions. *Geophys. Res. Lett.* **45**, 3737–3745 (2018).
9. Liu, L. *et al.* Uncertainty Quantification of Global Net Methane Emissions from Terrestrial Ecosystems Using a Mechanistically-based Biogeochemistry Model. *J. Geophys. Res. Biogeosciences* **125**(6), p.e2019JG005428. (2020).
10. McCalley, C. K. *et al.* Methane dynamics regulated by microbial community response to permafrost thaw. *Nature* **514**, 478–481 (2014).
11. Kelly, C. a, Carolina, N., Hill, C., Dise, B. & Martens, C. S. Temporal variations in the stable carbon isotopic composition of methane emitted from Minnesota peatlands. *Global Biogeochem. Cycles* **6**, 263–269 (1992).
12. Martens, C. S., Kelley, C. A., Chanton, J. P. & Showers, W. J. Carbon and hydrogen isotopic characterization of methane from wetlands and lakes of the Yukon-Kuskokwim Delta, Western Alaska. *J. Geophys. Res. Atmos.* **97**, 16689–16701 (1992).
13. Fisher, R. E. *et al.* Measurement of the <sup>13</sup>C isotopic signature of methane emissions from northern European wetlands. *Global Biogeochem. Cycles* **31**, 605–623 (2017).
14. Chasar, L. S., Chanton, J. P., Glaser, P. H. & Siegel, D. I. Methane concentration and stable isotope distribution as evidence of rhizospheric processes: Comparison of a fen and bog in the glacial Lake Agassiz Peatland complex. *Ann. Bot.* **86**, 655–663 (2000).
15. Nakagawa, F. *et al.* Stable isotope and radiocarbon compositions of methane emitted from tropical rice paddies and swamps in Southern Thailand. *Biogeochemistry* **61**, 1–19 (2002).
16. Conrad, R. *et al.* Stable carbon isotope discrimination and microbiology of methane formation in tropical anoxic lake sediments. *Biogeosciences Discuss.* **7**, 8619–8661 (2010).
17. Miller, J. B. & Tans, P. P. Calculating isotopic fractionation from atmospheric measurements at

- various scales. *Tellus, Ser. B Chem. Phys. Meteorol.* **55**, 207–214 (2003).
18. Higham, D. J. & Higham, N. J. *MATLAB guide*. vol. 150 (Siam, 2016).
  19. Qiu, C. *et al.* A strong mitigation scenario maintains climate neutrality of northern peatlands. *One Earth* (2022).
  20. Sherwood, O. A., Schwietzke, S., Arling, V. A. & Etiope, G. Global inventory of gas geochemistry data from fossil fuel, microbial and burning sources, version 2017. *Earth Syst. Sci. Data* **9**, 639–656 (2017).
  21. Holmes, M. E., Chanton, J. P., Tfaily, M. M. & Ogram, A. CO<sub>2</sub> and CH<sub>4</sub> isotope compositions and production pathways in a tropical peatland. *Global Biogeochem. Cycles* **29**, 1–18 (2015).
  22. Lan, X. *et al.* Improved Constraints on Global Methane Emissions and Sinks using  $\delta^{13}\text{C}$ -CH<sub>4</sub>. *Global Biogeochem. Cycles* (2021) doi:10.1029/2021gb007000.
  23. Deng, J. *et al.* Adding stable carbon isotopes improves model representation of the role of microbial communities in peatland methane cycling. *J. Adv. Model. Earth Syst.* **9**, 1412–1430 (2017).
  24. Burke, R. A., Barber, T. R. & Sackett, W. M. Methane flux and stable hydrogen and carbon isotope composition of sedimentary methane from the Florida Everglades. *Global Biogeochem. Cycles* **2**, 329–340 (1988).
  25. Burke Jr, R. A., Barber, T. R. & Sackett, W. M. Seasonal variations of stable hydrogen and carbon isotope ratios of methane in subtropical freshwater sediments. *Global Biogeochem. Cycles* **6**, 125–138 (1992).
  26. Conrad, R. Quantification of methanogenic pathways using stable carbon isotopic signatures: A review and a proposal. *Org. Geochem.* **36**, 739–752 (2005).
  27. Vaughn, L. J. S., Conrad, M. E., Bill, M. & Torn, M. S. Isotopic insights into methane production, oxidation, and emissions in Arctic polygon tundra. *Glob. Chang. Biol.* **22**, 3487–3502 (2016).
  28. King, S. L., Quay, P. D., Lansdown, J., M. The  $^{13}\text{C}/^{12}\text{C}$  Kinetic Isotope Effect for Soil Oxidation of Methane increase. *J. Geophys. Res.* **94**, 273–277 (1989).
  29. Chanton, J. P. The effect of gas transport on the isotope signature of methane in wetlands. *Org. Geochem.* **36**, 753–768 (2005).
  30. Zhang, G., Yu, H., Fan, X., Ma, J. & Xu, H. Carbon isotope fractionation reveals distinct process of CH<sub>4</sub> emission from different compartments of paddy ecosystem. *Sci. Rep.* **6**, 1–10 (2016).
  31. Janssens-Maenhout, G. *et al.* EDGAR v4. 3.2 Global Atlas of the three major Greenhouse Gas Emissions for the period 1970–2012. *Earth Syst. Sci. Data* **11**, 959–1002 (2019).
  32. Etiope, G. & Schwietzke, S. Global geological methane emissions: an update of top-down and bottom-up estimates. *Elem Sci Anth* **7**, (2019).
  33. Randerson, J. T., Chen, Y., Van Der Werf, G. R., Rogers, B. M. & Morton, D. C. Global burned area and biomass burning emissions from small fires. *J. Geophys. Res. Biogeosciences* **117**, (2012).
  34. Bergamaschi, P. *et al.* Satellite cartography of atmospheric methane from SCIAMACHY on board ENVISAT: 2. Evaluation based on inverse model simulations. *J. Geophys. Res. Atmos.* **112**, (2007).